Technical Report 32-1327

Aerodynamic Characteristics of Spherically Blunted 45-Deg Half-Angle Cones

R. Passamaneck

TECHNICAL REPORT 32-1327

Preface

The work described in this report was performed by the Environmental Sciences
Division of the Jet Propulsion Laboratory.

Page intentionally left blank

Contents

Tables

Figures

Contents (contd)

Figures (contd)

Contents (contd)

Abstract

Pressure, force, and dynamic stability tests were conducted to compare theoretically calculated coefficients and pressure distribution to data obtained by experiment. The Newtonian theory has also been included for completeness. Comparisons are made for an ideal gas and a real gas in equilibrium. The dynamic stability test for the real gas was omitted because of tunnel limitations. Pressure distribution was also measured for a real gas in nonequilibrium. The models used were 45-deg cones of bluntness ratios, R_N/R_B, of 0, 0.25, 0.50, 0.75, and 1.00.

Aerodynamic Characteristics of Spherically Blunted 45-Deg Half-Angle Cones

I. Introduction

A method of calculating the flow field about a body in unsteady flight has been reported in Ref. 1. The method uses a small perturbation technique in which the pitching velocity q, angle of attack α, the rate of change of q, and the rate of change of angle of attack are introduced to obtain perturbation from the steady state, axially symmetric flow field.

The computation is carried out in two parts. First a complete solution of the steady state, $\alpha = 0$, flow field in the shock layer is obtained by the method of characteristics. The starting line information for this solution is obtained by a blunt body flow analysis reported in Ref. 2. The second part of the solution is the unsteady flow field that results from the application of the perturbation scheme to the steady state solution. The form of the unsteady field, which is described as a function of angle of attack and pitching rate in cylindrical coordinates, is

$$P = P_0 + \left[P_{1,0}\,\alpha + P_{1,1}\frac{L}{V_\infty}\frac{d\alpha}{dt} \right] \cos\phi$$

$$+ \left[P_{1,2}\frac{L^2}{V_\infty}\frac{d^2\alpha}{dt^2} + \cdots \right] \cos\phi \qquad (1)$$

$$+ \left[\left(P_{2,0} - P_{1,0}\frac{X_{cg}}{L} \right)\frac{qL}{V_\infty} + \cdots \right] \cos\phi$$

The coefficient $P_{1,0}$ gives the first-order effect of a small, steady-state angle of attack on the pressure field, and $P_{1,1}$ and $P_{2,0}$ give the first-order effects of uniform plunging acceleration and pitching velocity, respectively. The stability derivatives result from the integration of the appropriate $P_{i,i}$ over the body surface. For example, $P_{1,0}$ can be integrated to obtain the static stability coefficients $C_{N\alpha}$ and $C_{M\alpha}$.

A detailed description of the method is given in Ref. 1 with results of a flow field calculation of a 10-deg cone at Mach number 10. A comparison of the calculation with experimental data for the 10-deg cone agrees reasonably well (Fig. 1).

The method of calculation was used by Kyriss and Rie to theoretically investigate the stability of an entry vehicle in model Mars atmospheres (Ref. 3). Three models of Mars and the earth's atmospheres were used to demonstrate the adaptability of the method to study flow fields of various mixtures of gases. The vehicles were cone, sphere cones, and power-law bodies. Most of the data presented was for sharp and spherically blunted 45-deg cones, and showed that both static and dynamic stability increased with increasing velocity (Fig. 2).

No experimental data were shown to verify the theoretical results. Therefore, it is the purpose of this investigation to experimentally determine the aerodynamic
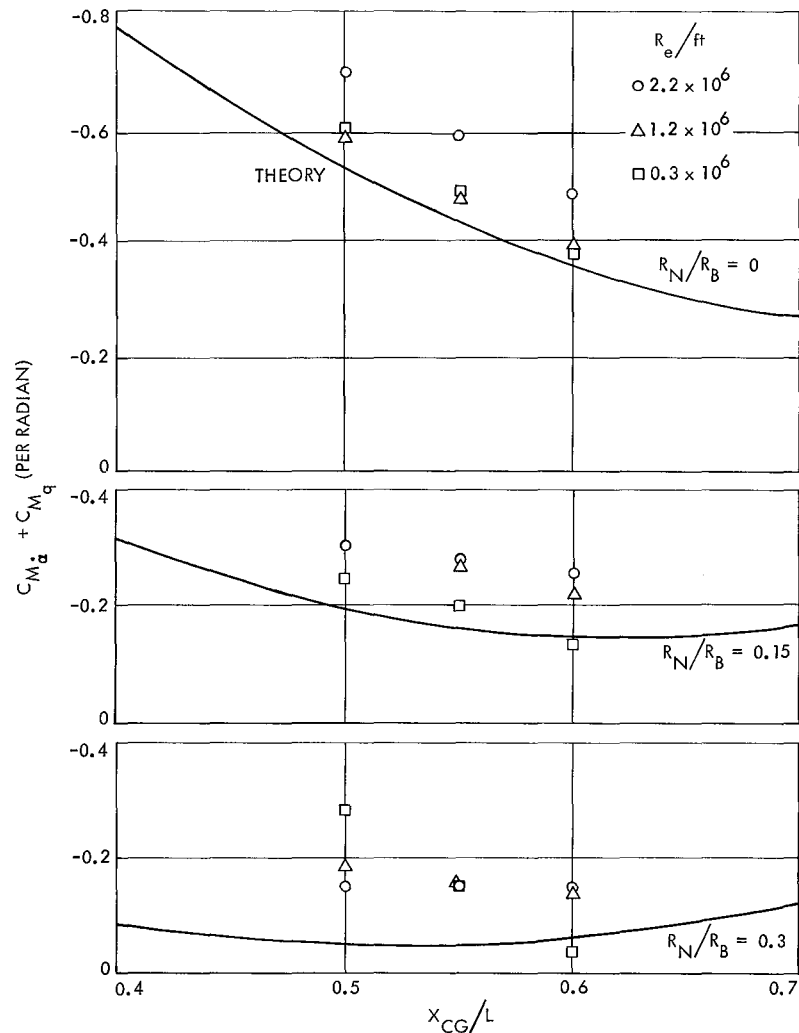
Fig. 1. Dynamic moment coefficient for flight in air, 10-deg sphere cone at M = 10, Ref. 3.

characteristics of a family of spherically blunted 45-deg cones and to compare the results with the theoretically calculated characteristics at the same flow conditions. A JPL subcontract (Ref. 4) was given to General Electric (GE) to calculate the aerodynamic characteristics for two flow conditions, one corresponding to an ideal gas and the other to a real gas in equilibrium.

II. Experimental Measurements

Because the aerodynamic characteristics are obtained by integration of the calculated pressure distribution, the prime objective of the experiment is to obtain pressure distribution at small angles of attack. This is done at several test conditions so as to investigate real gas effects

on the pressure distribution.[1] It has been reported (Ref. 5) that the bow shock wave moves closer to the body when real gas effects are considered present. The closer proximity of the shock wave causes the characteristics to be reflected back to the body more quickly, thus causing an adjustment of the pressure distribution. The models for the pressure measurements were 45-deg blunted cones with bluntness ratios, R_N/R_B, of 0.25 and 1.00. The 45-deg half-angle cone was selected because of the availability of theoretical data already published and, because of its

---

[1]The data from each phase of the report, the pressure and dynamic stability from JPL tests or the pressure and force from Wright-Patterson Air Force Base tests, can be obtained by writing directly to the author of this report, Jet Propulsion Laboratory, Pasadena, Calif.
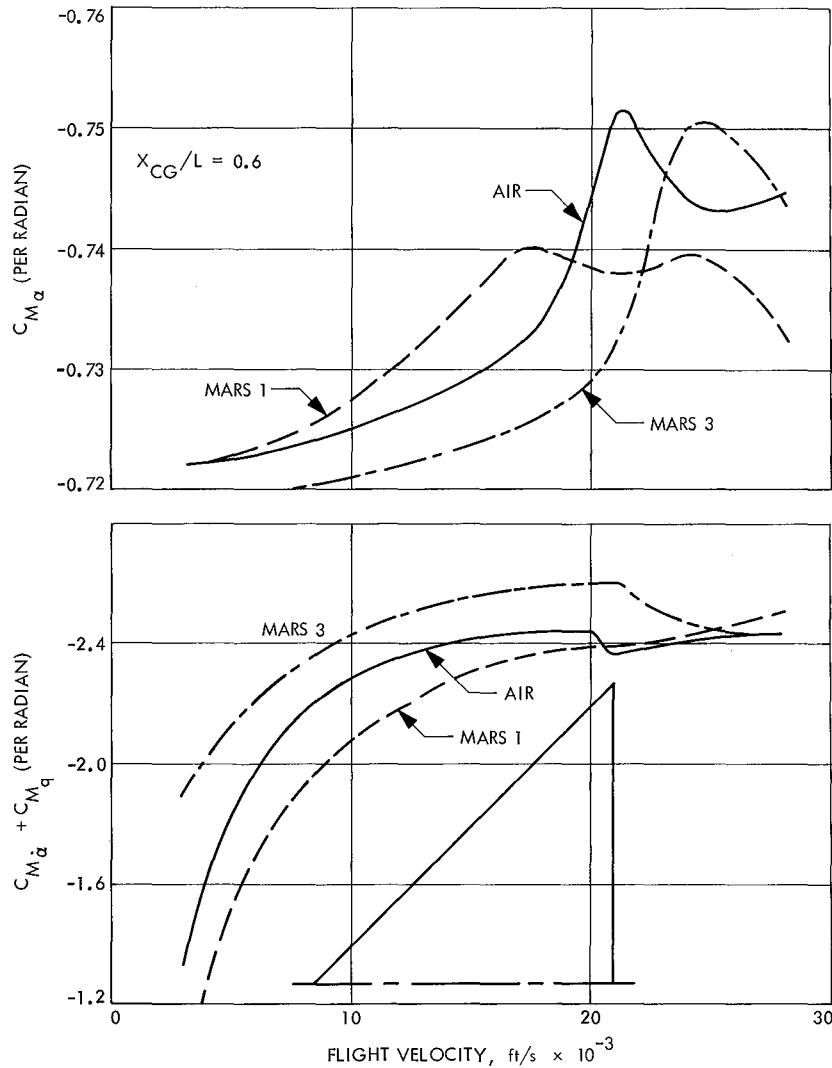
Fig. 2. Effect of flight velocity on moment coefficients for 45-deg pointed cone, Ref. 3

bluntness, it is a possible entry configuration. Cones of greater half angles result in subsonic flow over the model and, therefore, the theory is not applicable since the method of characteristics is employed in the analysis. Actually, for the ideal gas case, the flow on the conical surface was subsonic, and a small adjustment of density was made to establish supersonic flow (Ref. 4). Because of the effect of the real gas, this problem was not encountered in the real gas case. The theory is presently being extended to handle blunter configurations that have subsonic conical surfaces. The bluntness ratios of 0.25 and 1.00 were selected because they represent the extremes of the flow fields expected. The 0.25 bluntness ratio results in a conical flow being established aft of the spherical nose. With this configuration, the transition between spherical and conical flow can be obtained. The 1.00 bluntness ratio, which is a more probable entry con-

figuration, allows a more detailed study of the spherical flow field.

The models were tested under ideal gas conditions in the JPL hypersonic wind tunnel (HWT) and under real gas conditions, equilibrium air, in the 4-MW electro-gasdynamic facility at Wright-Patterson AFB, Dayton, Ohio. Both the ideal gas and real gas tests were run at a nominal Mach number of 10. Additional nonequilibrium runs were also made in the electro-gasdynamic facility (EGF).

A force test was also conducted in the EGF to obtain the static stability coefficients. A strain gage balance was used to measure axial forces, normal forces, and moments on the family of 45-deg half-angle cones with bluntness ratios of 0, 0.25, 0.50, 0.75, and 1.00. The force

test in the EGF was conducted instead of a dynamic stability test using a gas bearing because the gas bearing and EGF facility were incompatible. However, a dynamic stability test using the gas bearing was conducted in the HWT for the complete family of 45-deg half-angle cones.

III. Pressure Tests

The pressure tests were conducted in the HWT and EGF on 45-deg half-angle cones of bluntness ratios of 0.25 and 1.00. The angle-of-attack range was from −5 to +5 deg with roll angles, ϕ, of 0, 30, 60, and 90 deg. One pressure orifice was located on the opposite side of the model for a flow angularity check. Under these conditions, fairly complete model pressure distributions were obtained at each angle of attack. The measured pressures were non-dimensionalized by dividing by the pitot pressure. The pressure ratio was then plotted versus α and slopes were measured at $\alpha = 0$. These values of $1/P_{t_2} \, \partial P / \partial \alpha \, |_{\alpha=0}$ were then plotted versus S/R_N, where S is the surface distance from the nose of the model and R_N is the radius of the nose.

The models used for the pressure tests in the HWT are shown in Fig. 3. These models were made of steel with a base diameter of 5.5 in. The Mach number supply pressure and supply temperature were 10.08, 1500 cm Hg, and 1000°F, respectively. Data were taken for angle-of-attack increments of 0.5 deg. Supply pressure varied less than 2% during the test, supply temperature less than 1.03%, ϕ was set to within ±0.3 deg, and α was set to within ±0.005 deg. Based on repeatability of the data, the pressure, P/P_{t_2}, varied less than 1%. The pitot pressure, P_{t_2}, was calculated for a perfect gas flow at Mach 10. Since the actual test Mach number was 10.08, the calculated P_{t_2} is approximately 1% higher than the actual stagnation point pressure. This accounts for the stagnation point pressure ratio of 0.99 (Figs. 4 and 5).

Figures 6 and 7 show the pressure distribution for bluntness ratios of 0.25 and 1.00, respectively, at a nominal zero roll angle and various angles of attack. Excellent repeatability was obtained at each roll angle for $\alpha = 0$. It should be noted that an overexpansion occurred at the sphere-cone junction and that recompression to the sharp-cone value occurred on the 0.25 bluntness ratio model; however, recompression did not occur for the 1.00 bluntness ratio because the conical surface was too short. Pressure ratios for 40-, 45-, and 50-deg sharp cones are shown and it is evident that, for small angles of attack, pressures in the angle-of-attack plane can be predicted by using $\alpha = 0$ pressure of sharp cones whose surfaces make the angle with the flow. For example, the
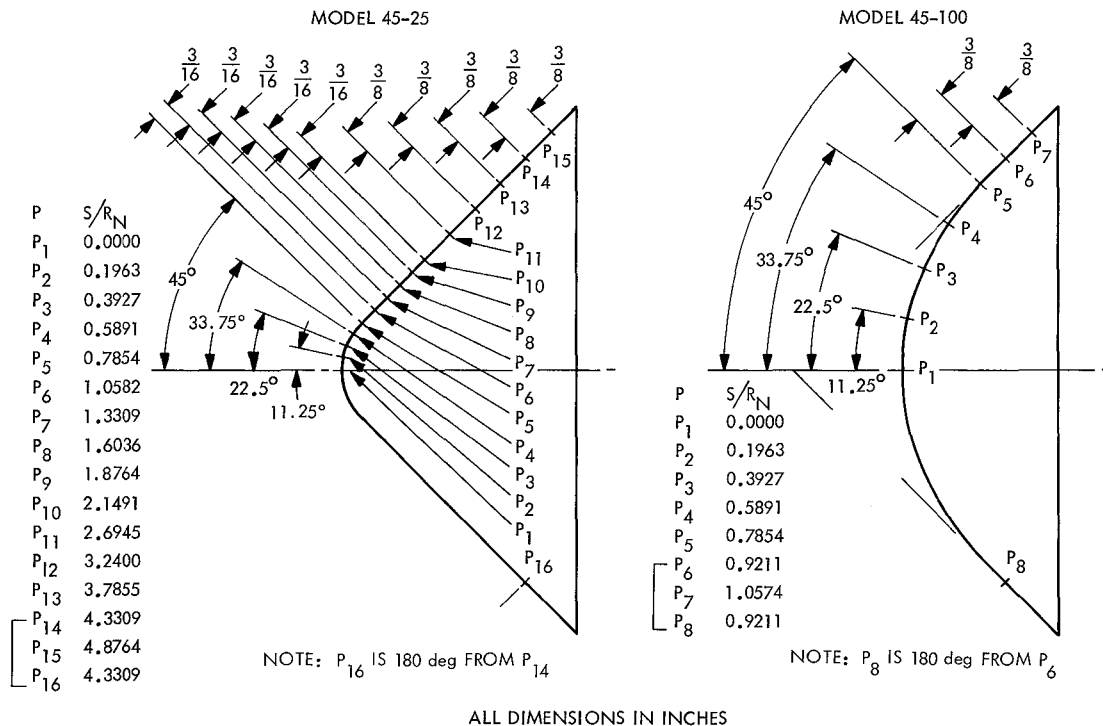
Fig. 3. Pressure models for hypersonic wind tunnel
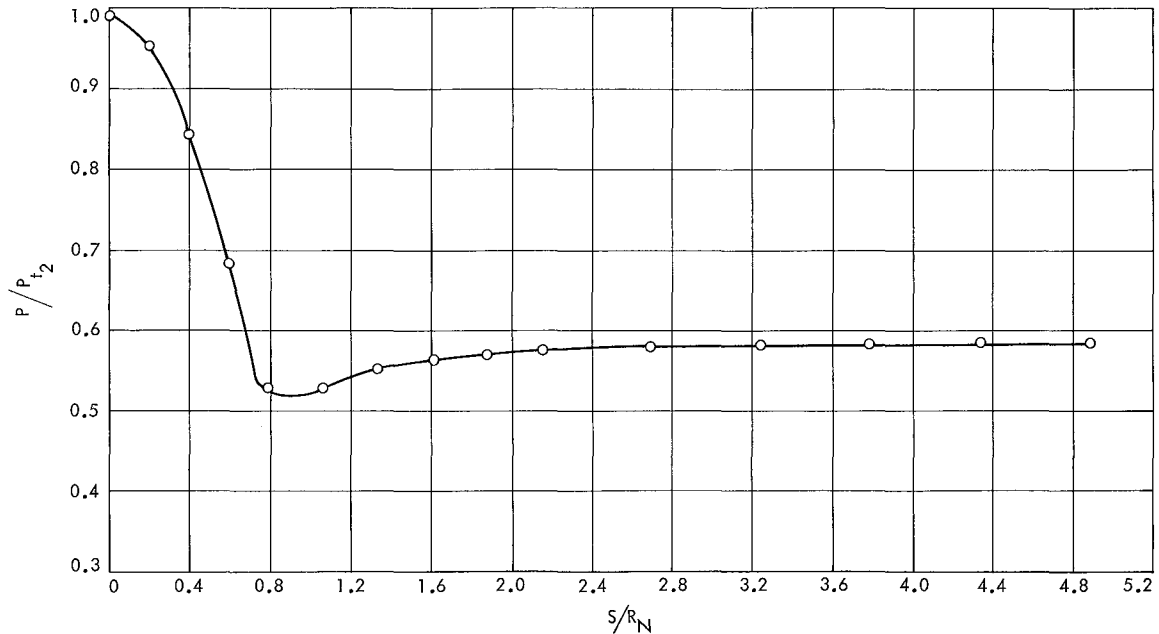
Fig. 4. Pressure ratio vs S/R_N for 45-25 model HWT at $\phi \cong 0$ deg and $\alpha = 0$ deg
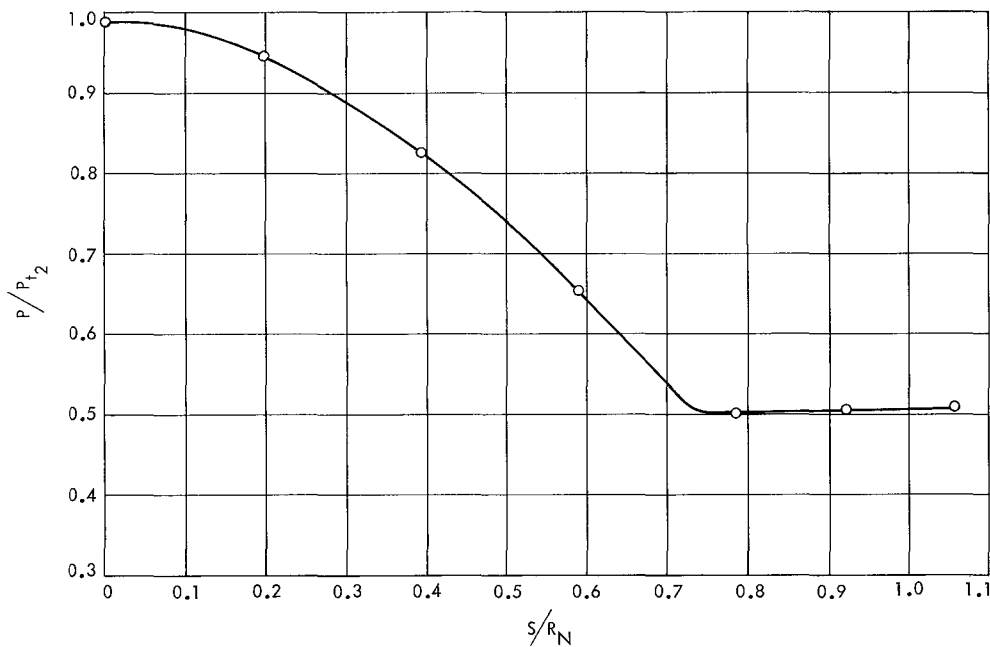
Fig. 5. Pressure ratio vs S/R_N for 45-100 model in HWT at $\phi \cong 0$ deg and $\alpha = 0$ deg

pressure on the windward surface for a 45-deg cone at −5 deg angle of attack is essentially the same at the pressure on a 50-deg cone at zero angle of attack.

It is interesting to note that the sonic point is near the sphere-cone junction at $\alpha = 0$. At angles of attack, the sonic point moves to the base of the model on the wind-ward side, but the pressure distribution indicates that supersonic conical flow occurs in the shock layer outside the "entropy" layer. The entropy layer is the layer of gas adjacent to the body that has passed through the normal part of the bow shock wave near the nose. An entropy gradient normal to the flow is characteristic of the "entropy" layer.
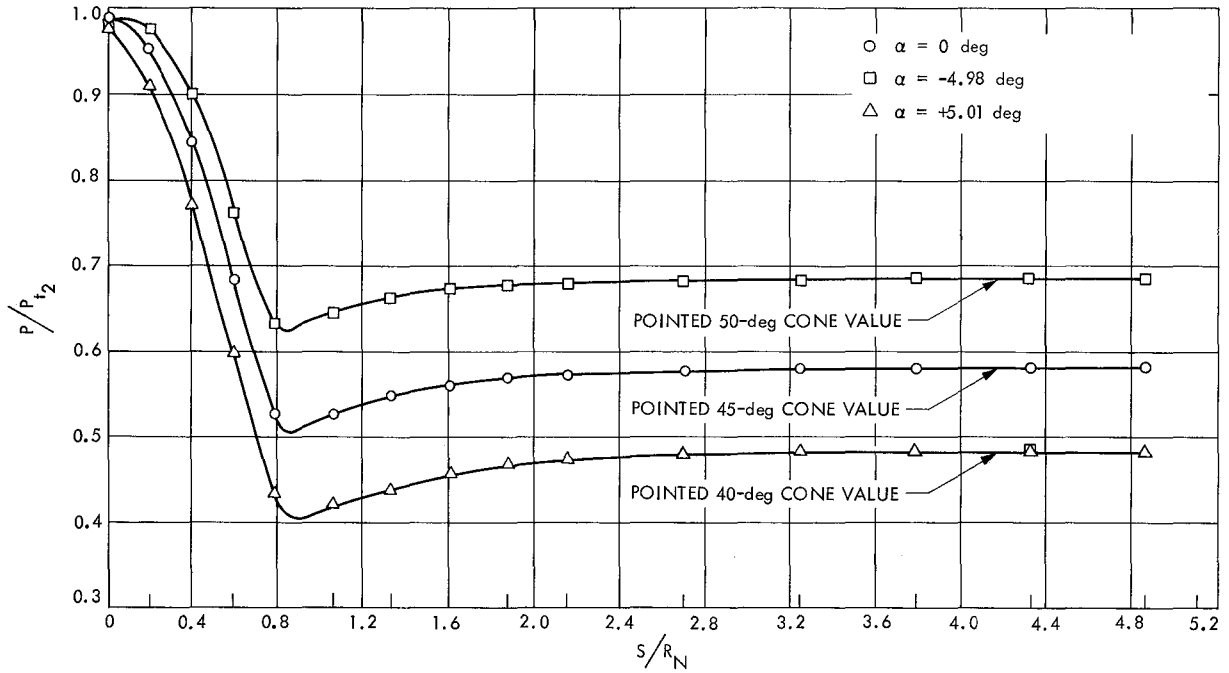
Fig. 6. Comparison of pressure ratio vs S/R_N for 45-25 model at $\alpha = -5, 0,$ and $+5$ deg at $\phi = 0$ deg in HWT
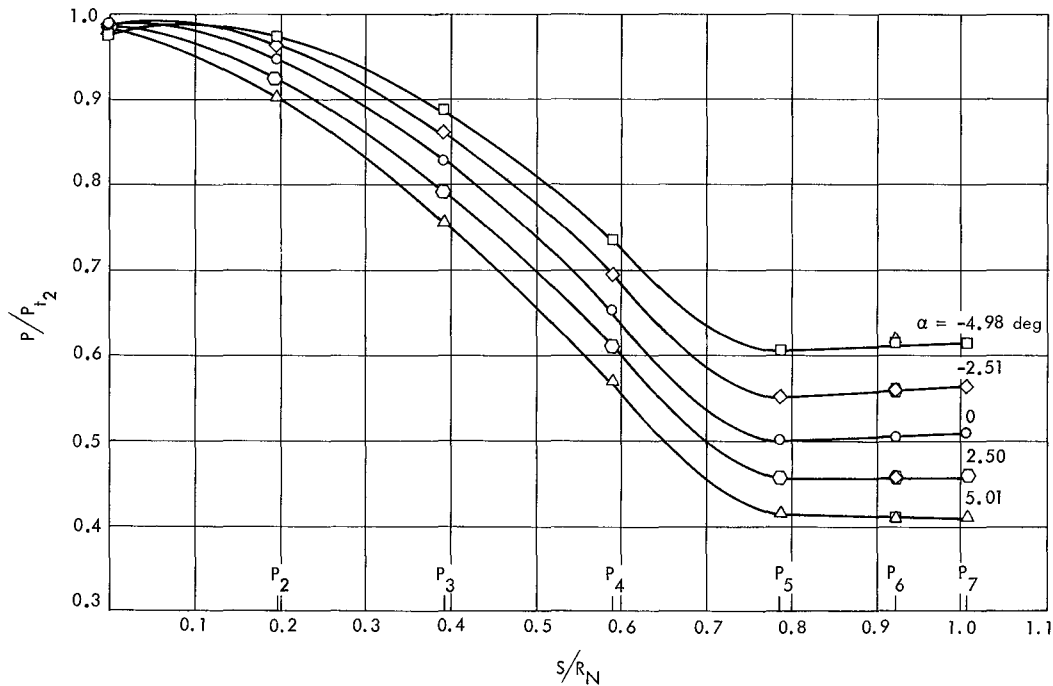
Fig. 7. Comparison of pressure ratio vs S/R_N for 45-100 model at $\alpha = -5, -2.5, 0, +2.5,$ and $+5$ deg at
$\phi = 0$ deg in HWT

A typical plot of pressure ratio versus angle of attack is shown in Fig. 8. Only the first five orifices are shown for clarity since the other orifices indicate pressures which are equal to P_5. The linearity with α is good on the leeward side ($+\alpha$) and is slightly nonlinear on the windward side ($-\alpha$) as the base of the model is approached.
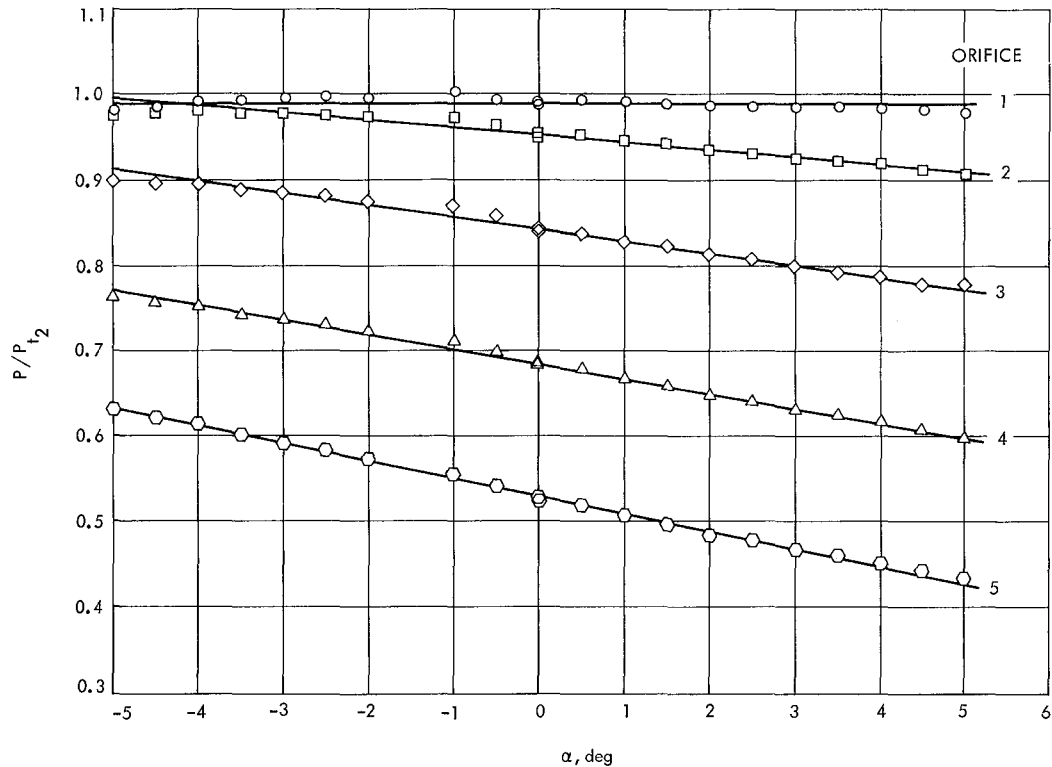
Fig. 8. Pressure ratio vs α for 45-25 model at ϕ = 0 deg in HWT

Figures 9 and 10 show the pressure ratio slopes, $1/P_{t_2} \, \partial P / \partial \alpha \, |_{\alpha=0}$, as a function of body position for bluntness ratios of 0.25 and 1.00, respectively. The Newtonian theory has been included for comparison. For each roll angle, except ϕ = 90 deg, the experimental values are less than the Newtonian values.

The models used in the EGF were made of alumina to withstand the high temperatures. The alumina models are formed by a casting process and, therefore, the location of the pressure orifices could not be held to the same tolerances as for the steel models used in the HWT tests. The models had a base diameter of 2.0 in. This diameter was dictated by the core size of the test flow in the EGF. The models, with orifice locations, are shown in Fig. 11. As in the HWT pressure tests, a single orifice was located 180 deg from the primary orifices for a flow angularity check. However, the uncertainty of the orifice location makes this check questionable.

The 4-MW electro-gasdynamic facility was selected because it can produce near-equilibrium flow conditions in the test section for a Mach number of 10 and altitude of 160,000 ft. Whether or not the test medium is in equilibrium has been investigated and reported in Ref. 6. The conclusion drawn, based on tests with a circular cylinder normal to the flow, was that reliable blunt body pressure data can be obtained with little concern for the detailed thermo-chemical state of the gas. However, this may not be the case for other blunt bodies where the pressure distribution may be affected by the location of the shock wave. Since the effect of the thermo-chemical state of the gas is uncertain, tests were also run at nonequilibrium free-stream conditions for comparison.

Two test conditions were run. One was a near-equilibrium condition with P_t = 1690 psia and H_0 = 2400 btu/lb$_m$; this is the Mach 10, 160,000-ft altitude condition previously mentioned. The other condition has nonequilibrium test flow with P_t = 525 psia and H_0 = 2800 btu/lb$_m$. A description of the tunnel and instrumentation is given in Ref. 7 and the flow analysis and calibration are given in Ref. 8. The test conditions are tabulated in Table 1. Test conditions are more difficult to repeat in the EGF than in the HWT and are more difficult to maintain during the run. However, the variation in supply pressure during a run was generally less than 1% and variation in total enthalpy was less than 8%. The nominal angles of attack at which data were taken were -5, -3, -1, 0, $+1$, $+3$, and $+5$ deg. The angle of attack was set to within ±0.1 deg. The roll angles, ϕ, were the same as those for the HWT test, i.e., ϕ = 0, 30, 60, and 90 deg.

Fig. 9. $1/P_{t_2} \partial P/\partial \alpha \mid_{\alpha=0}$ vs S/R_N for 45-25 model at $\phi = 0, 30, 60,$ and 90 deg in HWT with Newtonian theory

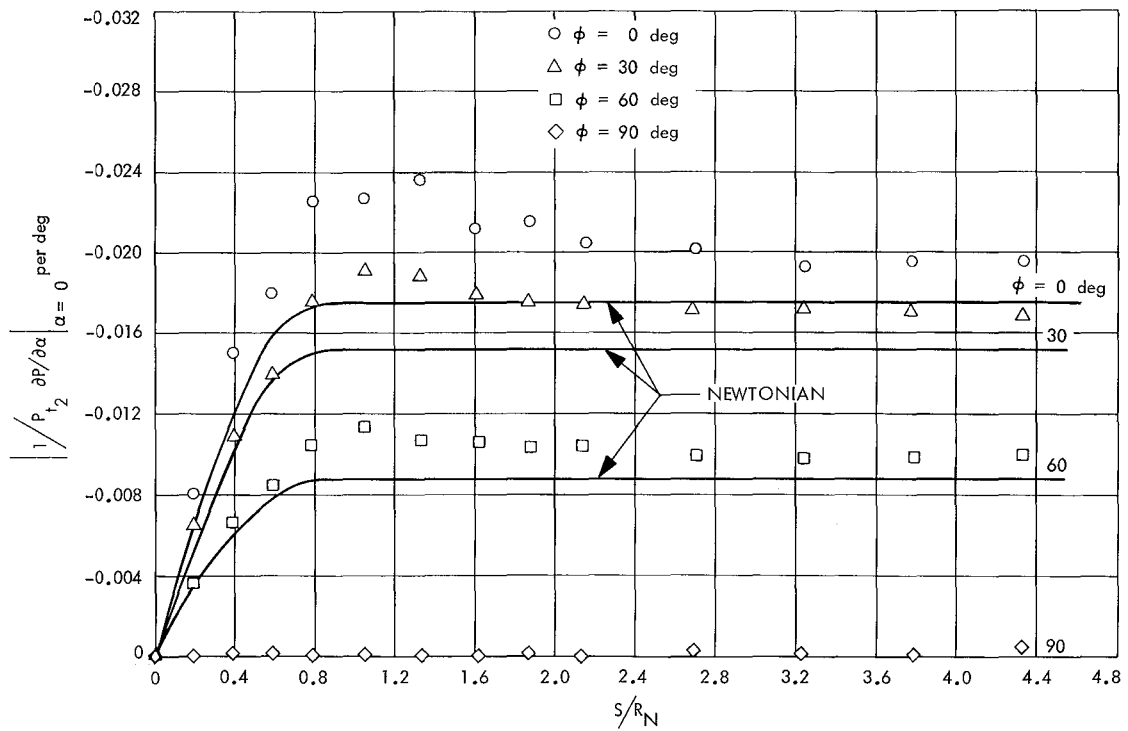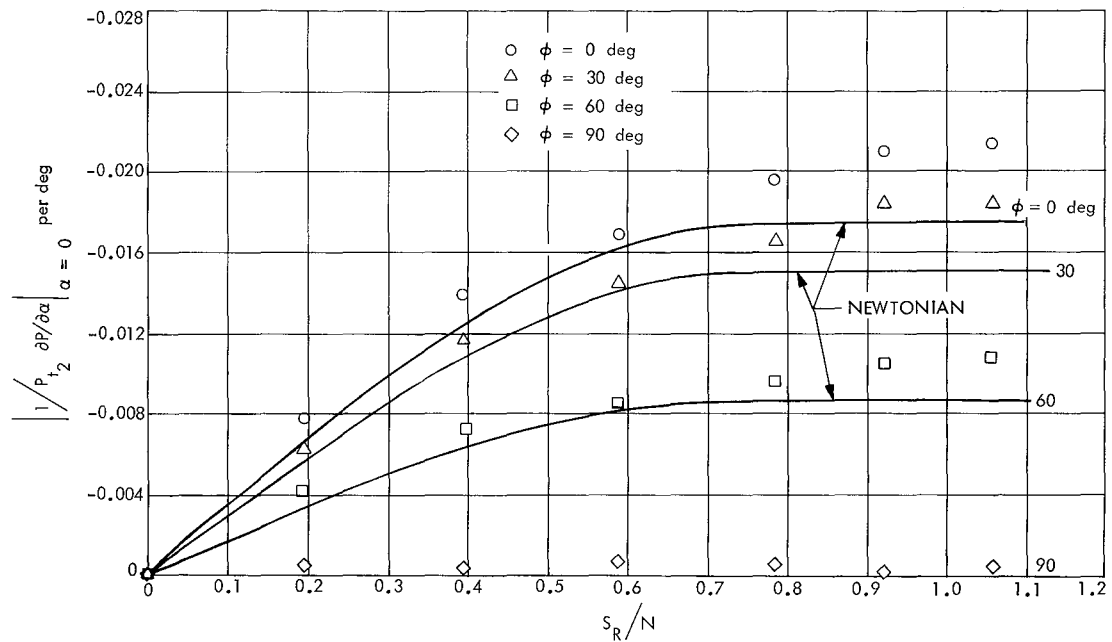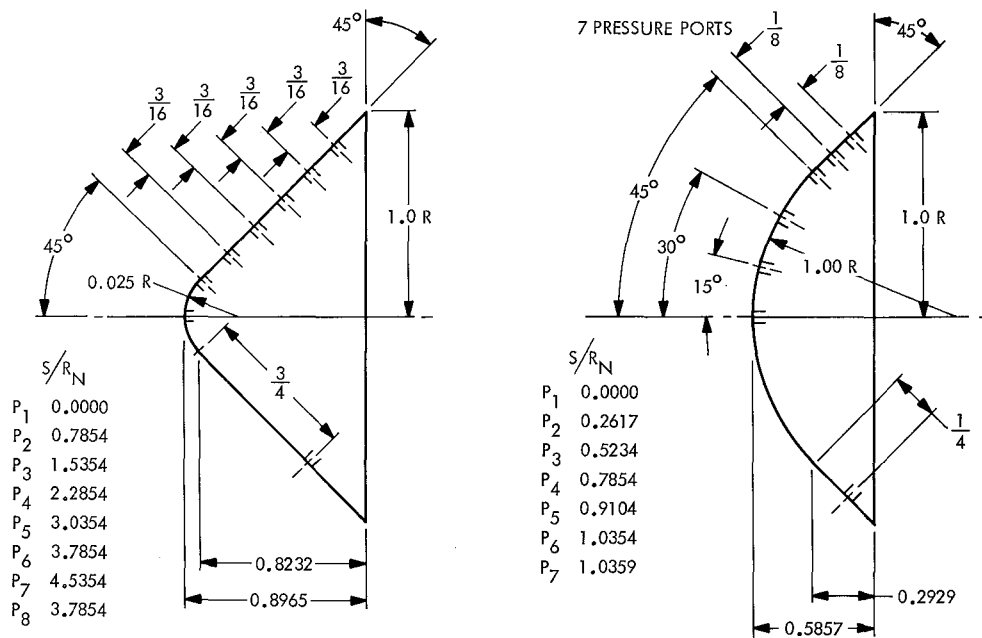Fig. 10. $1/P_{t_2} \partial P/\partial \alpha \mid_{\alpha=0}$ vs S/R_N for 45-100 model at $\phi = 0, 30, 60,$ and 90 deg in HWT with Newtonian theory

ALL DIMENSIONS IN INCHES

Fig. 11. Pressure models for the EGF

Three runs were made with bluntness ratio of 1.00 at $\phi = 60$ deg. These data are plotted and show that the largest data scatter occurs at the stagnation point and decreases with distance along the model (Fig. 12). An estimate of the repeatability can also be made from this plot. A separately measured P_{t_2} did not correlate with the supply pressure as well as did the model stagnation pressure, $P_{1,0}$; therefore, the data was non-dimensionalized by dividing by $P_{1,0}$. The pressure ratio for the 45-100 model at $\alpha = 0$ is plotted vs S/R_N (Fig. 13). The large data scatter did not seem to be consistent with the scatter indicated in Fig. 12; therefore, it was decided to average the data at the repeated runs (Fig. 14 resulted). $\bar{P}$ is the average of the repeated data at $\alpha = 0$ at each orifice location. $\bar{P}_1$ is the average of all the P_1 at a given roll angle. It includes the P_1 at angle of attack, since P_1 should vary only approximately 1% throughout the angle-of-attack range.

The pressure distribution for the 45-100 model at $\alpha = 0$ for the nonequilibrium is shown in Fig. 15. The pressure distributions for the 45-25 model at $\alpha = 0$ for the near-equilibrium and nonequilibrium cases are shown in Fig. 16. The HWT data have been included for comparison. The ideal gas data obtained in the HWT and the nonequilibrium data obtained in the EGF agree reasonably well while the near-equilibrium data obtained in the EGF are somewhat lower. This was also the case for the 45-100 model (Fig. 14), which appears to indicate

that the thermo-chemical state of the gas has an important effect on the pressure distribution.

The plots of $P/P_{1,0}$ versus α were fairly linear for all the nonequilibrium cases except for the 45-25 model at $\phi = 90$ deg. A typical plot of this case is shown in Fig. 17. For the equilibrium case, the data for both models showed considerable scatter, with $\phi = 0$ deg for the 45-25 model being the worst case. The slopes of the pressure ratio versus S/R_N for the 45-25 model at $\phi = 0$, 30, and 60 deg are shown in Fig. 18. The variation in slope due to data scatter for $\phi = 0$ (the worst case) has been included to indicate data quality. The Newtonian values for the three roll angles have been included for comparison. The data for $\phi = 60$ deg agree reasonably well with the Newtonian curve, while the data for $\phi = 30$ deg agree with the Newtonian curve near the sphere-cone junction and then approach the curve for $\phi = 60$ deg on the conical part of the model. The pressure ratio slopes for the 45-100 model for the near-equilibrium and the nonequilibrium cases are shown in Figs. 19 and 20, respectively. The curves are the Newtonian values and have been included for comparison. The data are incomplete because some of the data were omitted due to the large amount of scatter on the spherical nose. This was particularly true at $\phi = 0$ deg. It can be seen that the nonequilibrium data agree better with Newtonian theory than the near-equilibrium data. This had been previously obtained for the 45-25 model in Fig. 16.

Table 1. Test conditions for real gas test

Model	ϕ, deg	P_0, psia	H_0, Btu/lbm	P_{t_2}, psia	P_1, min Hg	Flow condition
Pressure						
45-25	0	1700.161	2402	2.014	100.215	near-equilibrium
	30	1724.503	2389	1.967	99.747	
	60	1686.629	2194	2.010	87.921	
	90	1675.909	2158	2.890	91.446	
45-100	0	1673.808	2375	1.998	88.363	
	30	1681.520	2367	2.682	92.973	
	30	1712.124	2385	2.479	82.502	
	60	1667.245	2330	2.404	84.258	near-equilibrium
	60	1669.884	2061	1.892	83.858	
	60	1679.612	2304	2.094	94.259	
	90	1672.306	2294	1.817	88.319	
45-25	0	525.258	2606	2.460	105.338	
	30	533.027	2769	3.825	109.981	
	60	526.259	2800?	3.364	102.486	
	90	523.310	2800?	2.323	100.269	non-equilibrium
45-100	0	552.954	2527	3.550	110.808	
	30	517.782	2713	2.430	97.496	
	60	521.178	2807	3.416	102.546	
	90	518.271	2798	2.536	99.952	
Force						
45-00		1725	2550			
45-25		1747	2200			
45-50		1702	2250			
45-75		1685	2600			
45-100		1700	2630			
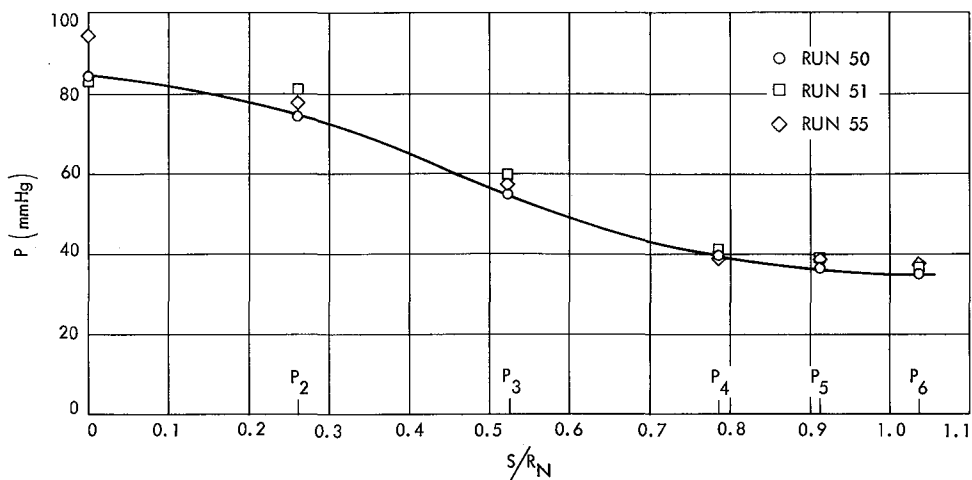
Fig. 12. Pressure ratio vs S/R_N for 45-100 model in EGF at $\alpha = 0$ deg and $\phi = 60$ deg for identical conditions for data repeatability estimate (equilibrium flow)
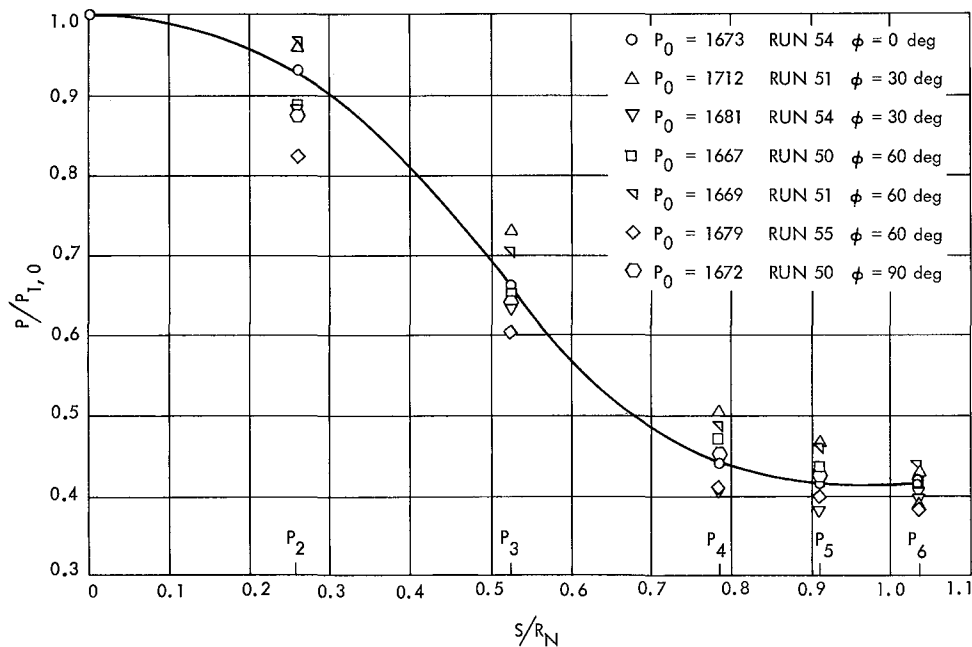
Fig. 13. Pressure ratio vs S/R_N for 45-100 model in EGF at $\alpha = 0$ deg and various roll angles indicate scatter (equilibrium flow)
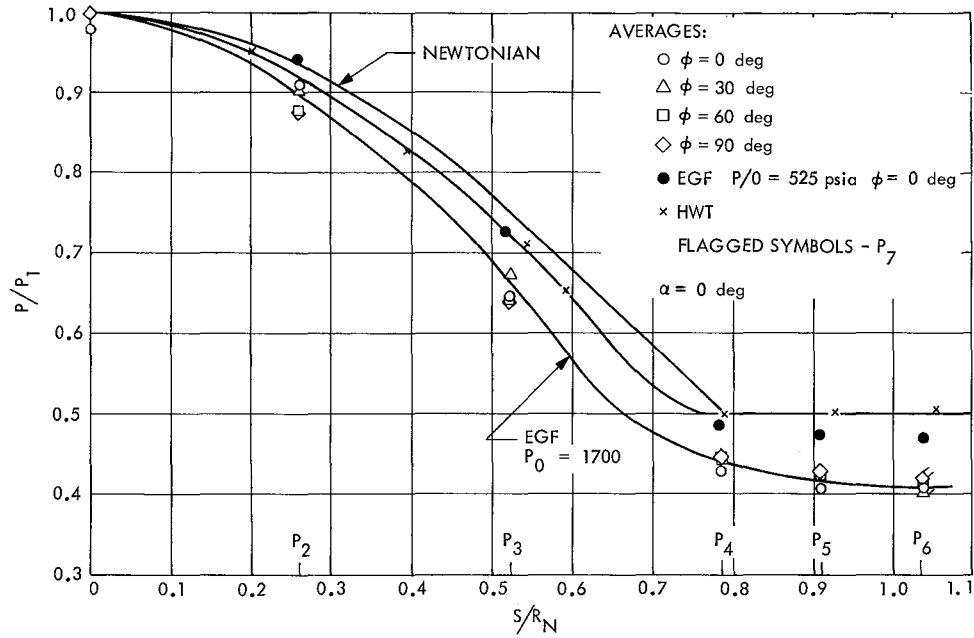
Fig. 14. Comparison of Newtonian, HWT, and EGF pressure ratios vs S/R_N for 45-100 model
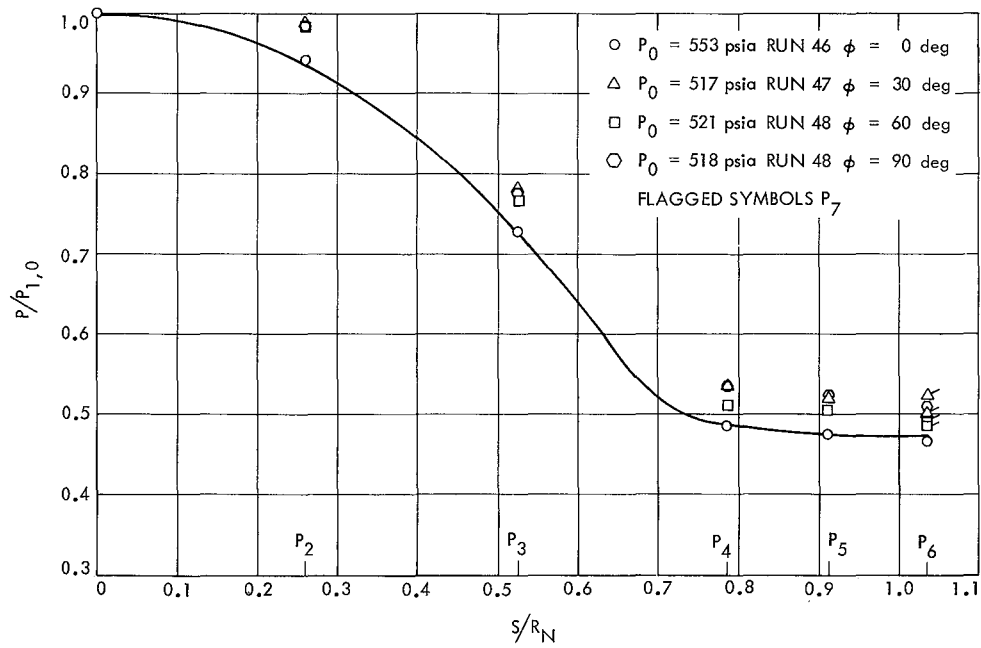
Fig. 15. Pressure ratio vs S/R_N for 45-100 model in EGF at $\alpha = 0$ deg (nonequilibrium flow)
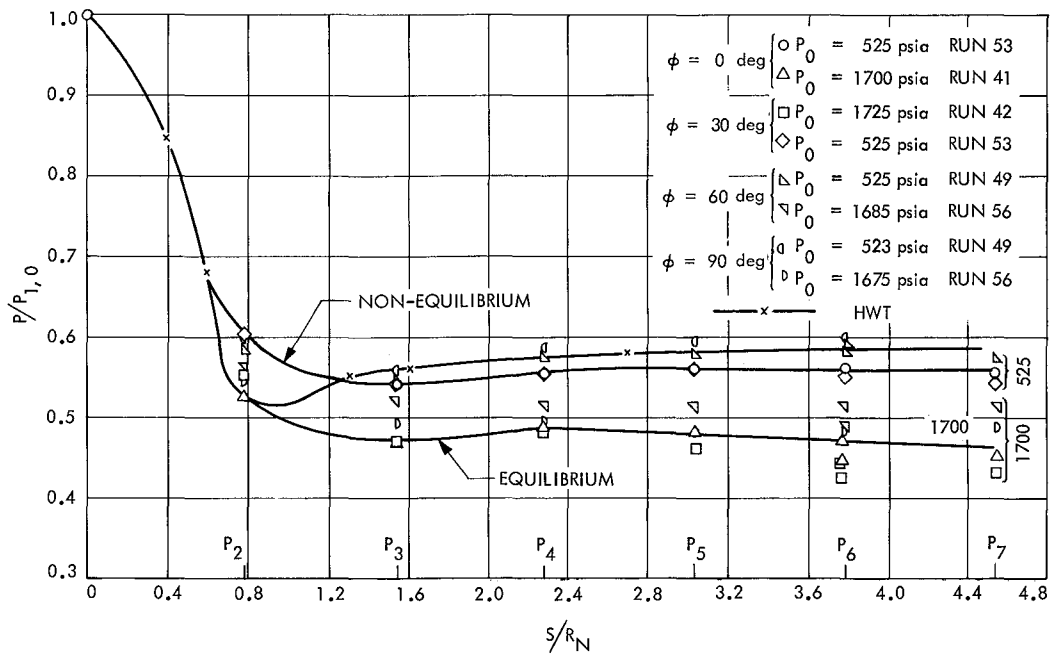
Fig. 16. Comparison of HWT, EGF (equilibrium), and EGF (nonequilibrium) pressure ratios vs S/R_N for 45-25 model
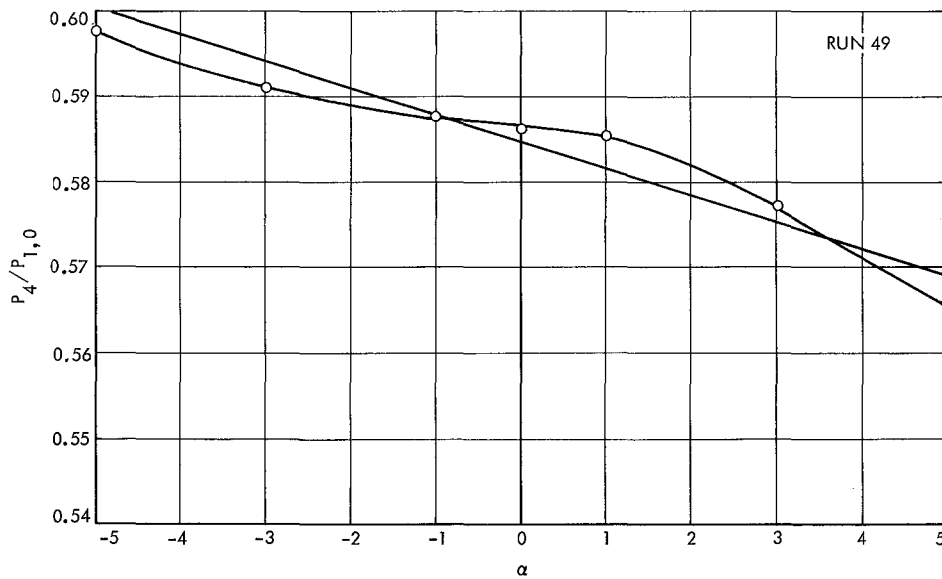
Fig. 17. Pressure ratio vs α for 45-25 model at $\phi = 90$ deg in EGF (nonequilibrium)
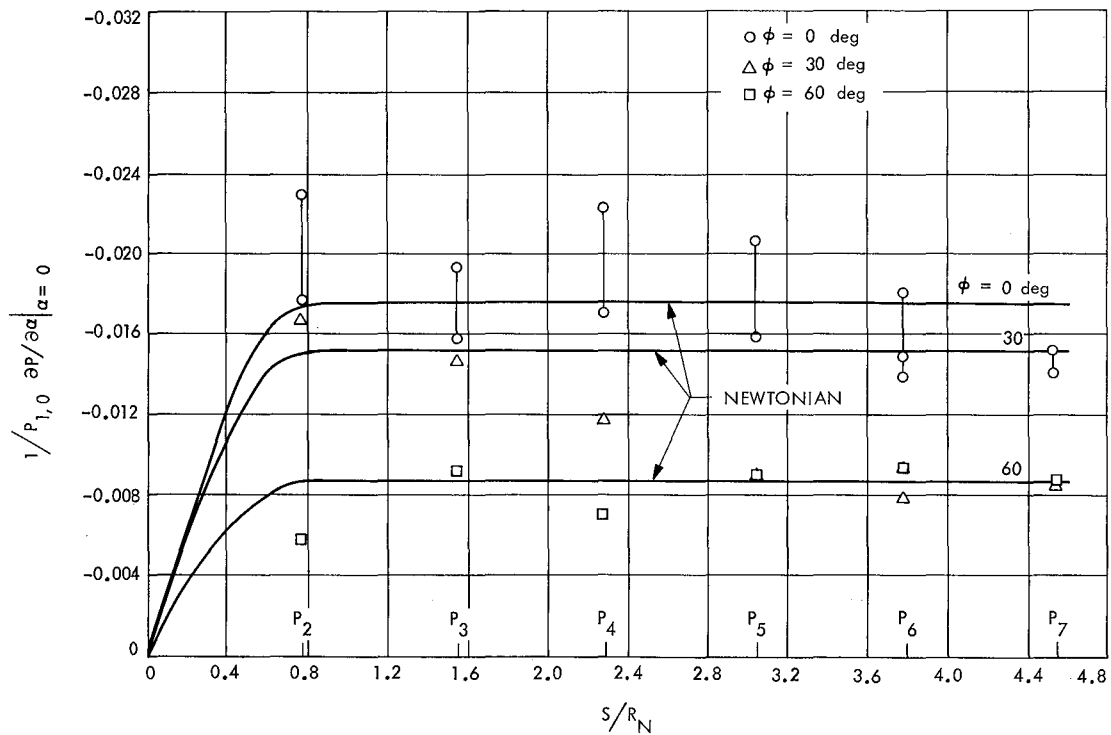
Fig. 18. $1/P_{t_2} \partial P/\partial \alpha \big|_{\alpha=0}$ vs S/R_N for 45-25 model at $\phi = 0$, 30, and 60 deg in EGF (equilibrium) with Newtonian theory
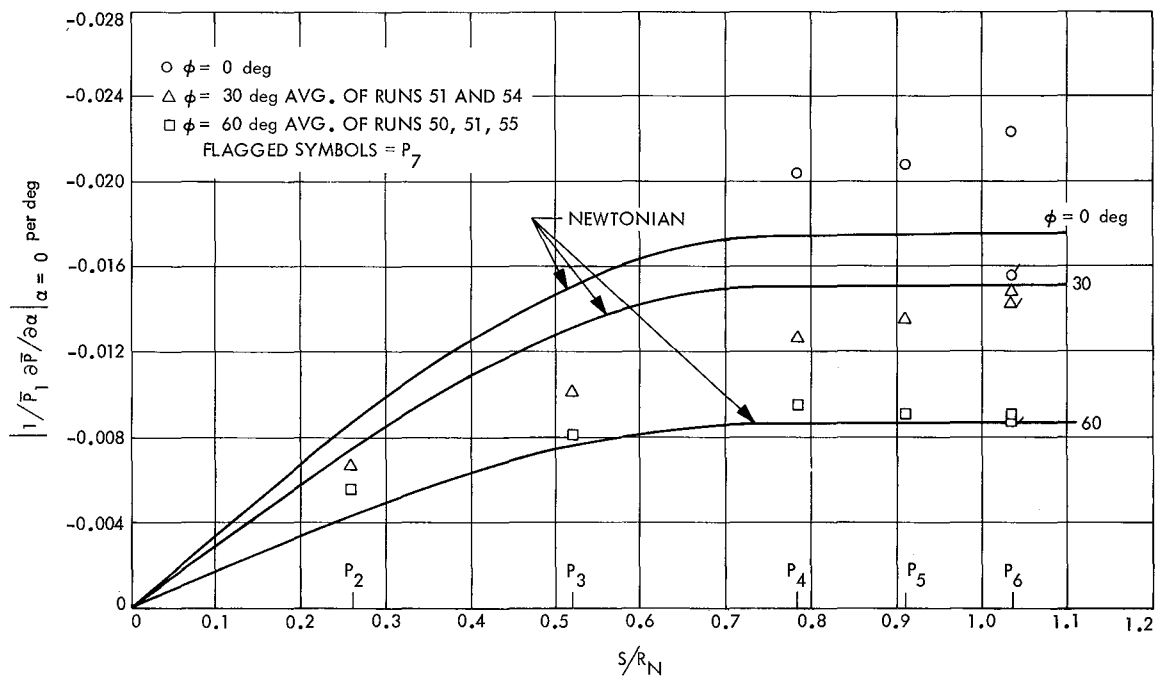
Fig. 19. $1/P_{t_2} \partial P/\partial \alpha \big|_{\alpha=0}$ vs S/R_N for 45-100 model at $\phi = 0$, 30, and 60 deg in EGF (equilibrium) with Newtonian theory
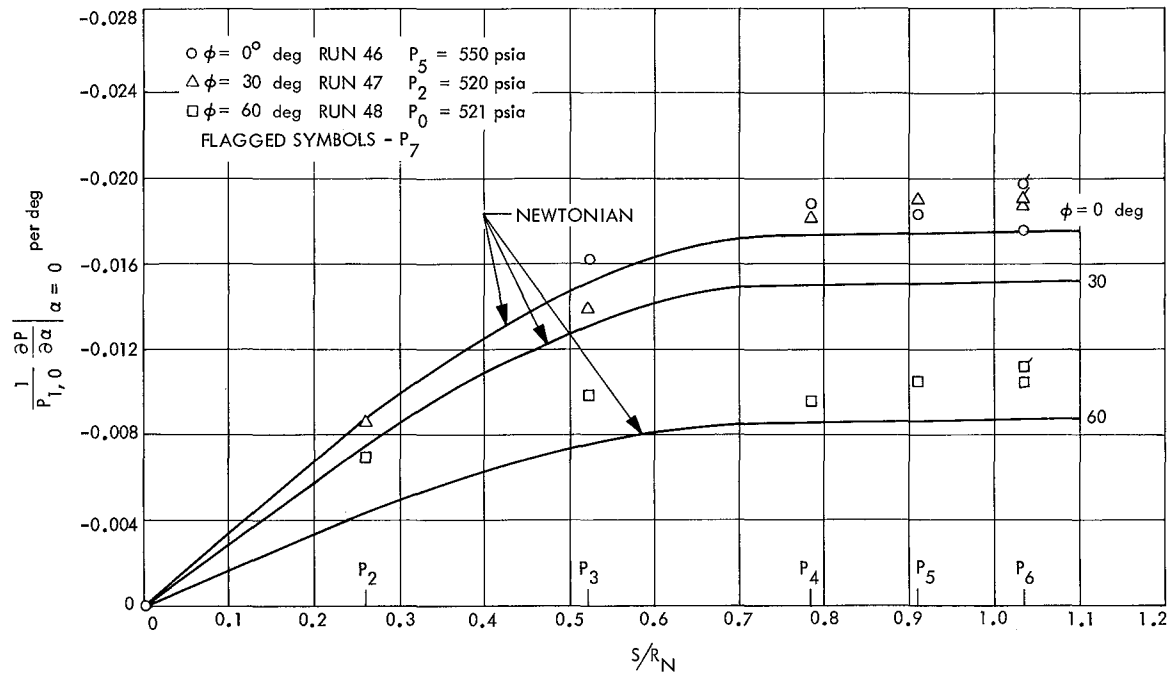
Fig. 20. $1/P_{t_2} \partial P/\partial \alpha \mid_{\alpha=0}$ vs S/R_N for 45-100 model at ϕ = 0, 30, and 60 deg in EGF (nonequilibrium) with Newtonian theory

IV. Force Tests

Force tests were conducted in the EGF at the same flow conditions as the pressure tests. A strain gage balance was used to measure the normal and axial forces and the pitching moments on the models. The models were 2.0-in.-diam 45-deg half-angle cones with bluntness ratios of 0, 0.25, 0.50, 0.75, and 1.00. The angle-of-attack range and schedule was the same as that used in the pressure tests. The test conditions are tabulated in Table 1.

Unfortunately, the pitot pressure and mass flux, $\rho_\infty U_\infty$, were not measured during the force tests at the EGF. However, using the results of the pressure tests, run at the same conditions, the ratio of pitot pressure to total pressure was calculated. After calculating this ratio and measuring total enthalpy, the Mach number could be obtained by using Ref. 9. The Mach number for the pressure tests remained at an essentially constant value of 10.2. Again, referring to Ref. 9 and using $M = 10.2$ as a parameter, the ratio of dynamic pressure to total pressure was plotted vs the total enthalpy (Fig. 21). It is obvious that q_∞, the normalizing quantity needed to find force coefficients and moment coefficients, can be obtained if the total pressure and enthalpy are known. This procedure leaves much to be desired; however, it was the only

course left open to reduce the data. No reference was known to exist in which the procedure applied above could be used to find the dynamic pressure for the non-equilibrium test condition. It is for this reason that the coefficient form for the nonequilibrium data cannot be given. The comparison of equilibrium as well as non-equilibrium to theory falls short in this respect.

A typical plot of axial force coefficient versus angle of attack for the equilibrium test gas is shown in Fig. 22. The effect of angle of attack on C_A was lost in data scatter for all cases. The axial force coefficient at zero angle of attack has been plotted versus bluntness ratio in Fig. 23, with the scatter bands being the maximum and minimum values of C_A over the entire angle-of-attack range. No base pressure correction was made.

A typical plot of normal force coefficient versus angle of attack is shown in Fig. 24. There was very little scatter in the data, and a linear curve represents the data well.

A typical plot of pitching moment coefficient versus angle of attack is shown in Fig. 25. Although the pitching moments were small, the data appeared to be of high quality and linear curves represent the data well.
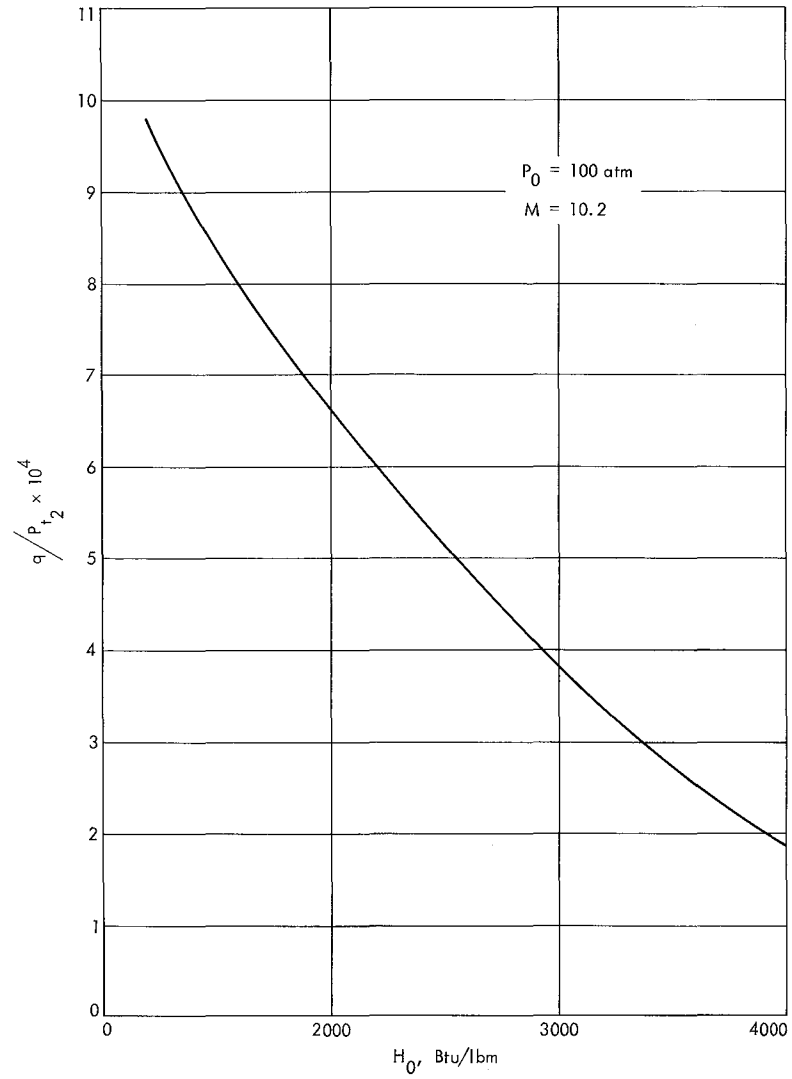
Fig. 21. q/P_t vs H_0 for equilibrium in air, Ref. 9

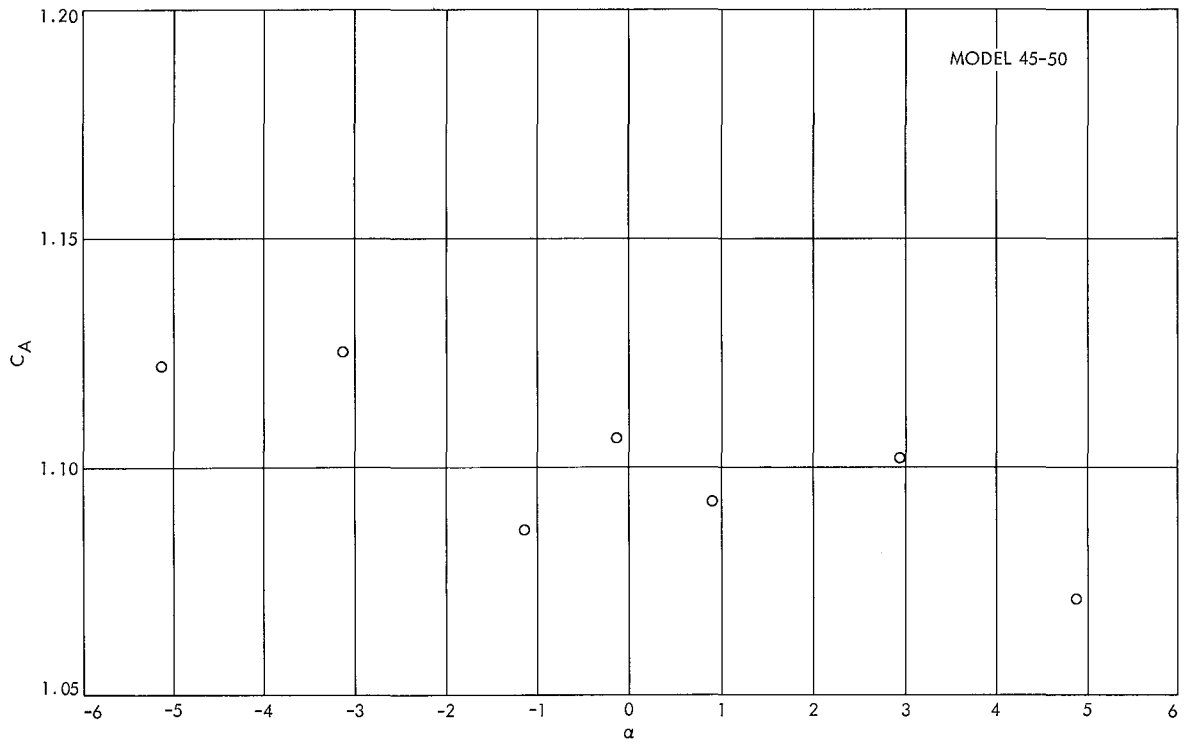**Fig. 22. Typical plot of axial force coefficient, C_A, vs α for EGF (equilibrium)**
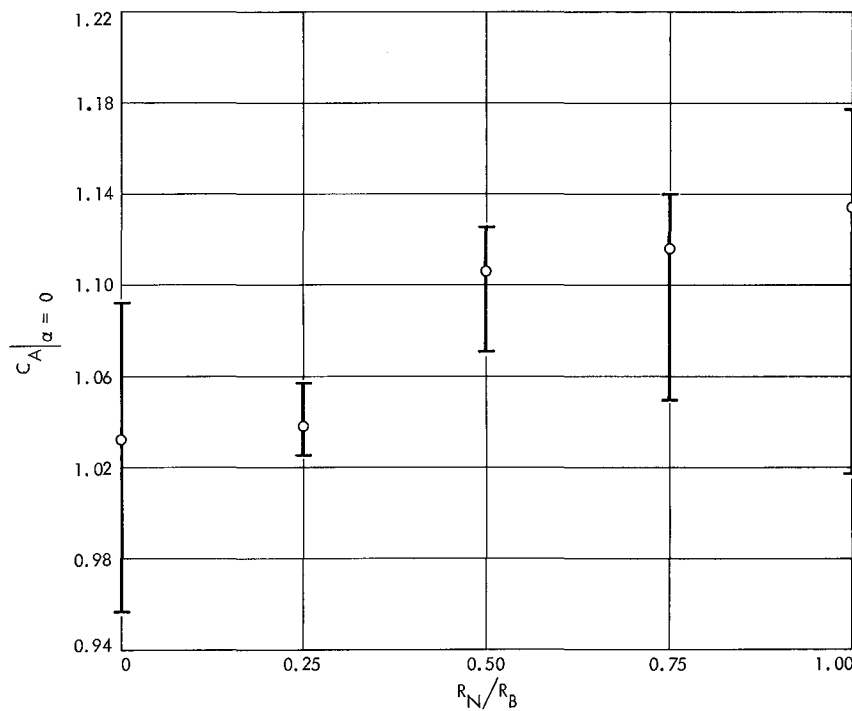
Fig. 23. $C_A \big|_{\alpha=0}$ vs R_N/R_B for EGF (equilibrium)
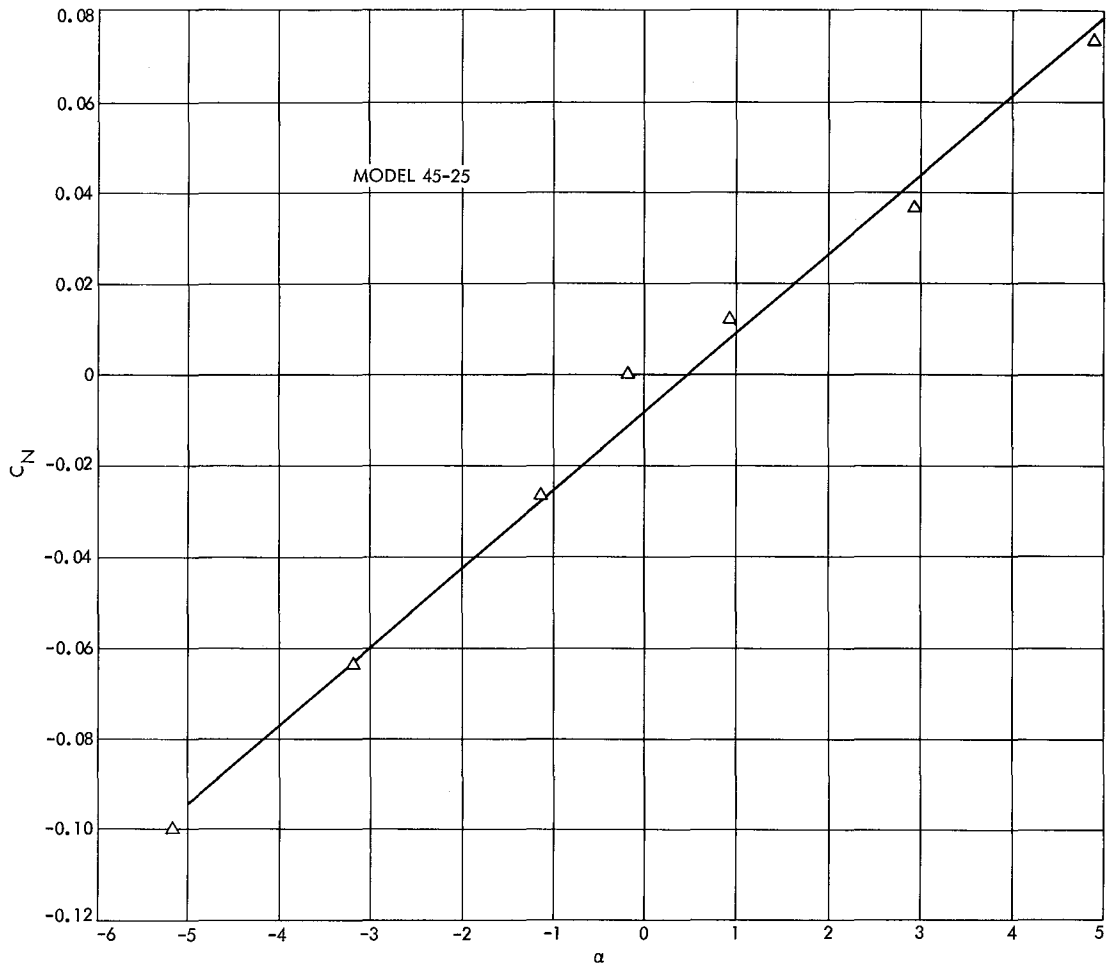
Fig. 24. Typical plot of normal force coefficient, C_N, vs α for EGF (equilibrium)
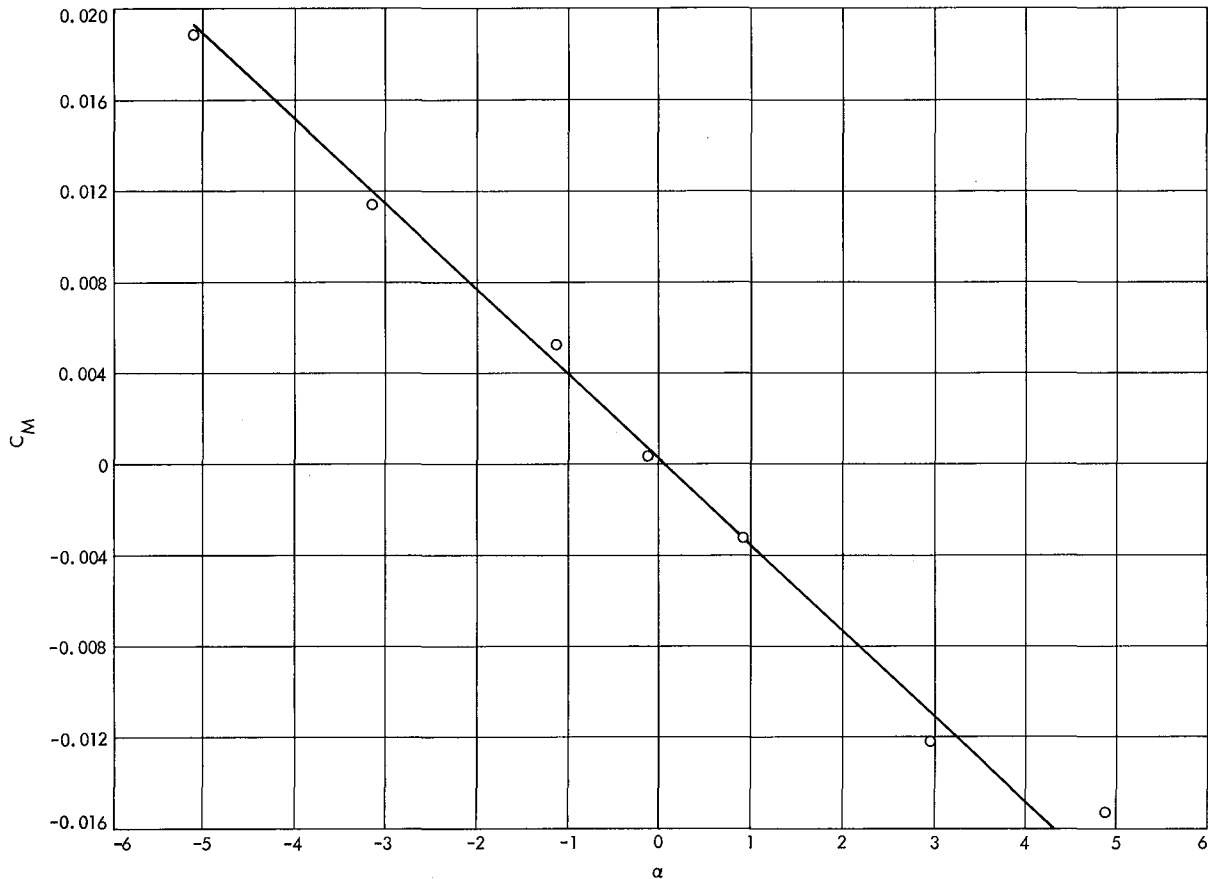
Fig. 25. Typical plot of moment coefficient, C_M, vs α for EGF (equilibrium)

V. Dynamic Stability Test

The static and dynamic stability of models were measured in the JPL HWT using a sting-mounted gas bearing and Optron Tracker. The testing technique and data reduction are described in Ref. 10. The test Mach number was 10.13, supply pressure was 1500 m Hg, and supply temperature was 1515°R.

To accommodate the gas bearing and locate the CG at the base of the cone, a hemispherical shell was attached to the base of the model. This also provided the color contrast marking needed for the Optron Tracker. Figure 26 shows a typical test setup. The diameter of the hemisphere was less than the base diameter of the cone to prevent afterbody effects on the cone stability.

Moments of inertia of the models were measured before the tests and are tabulated in Table 2. Since the
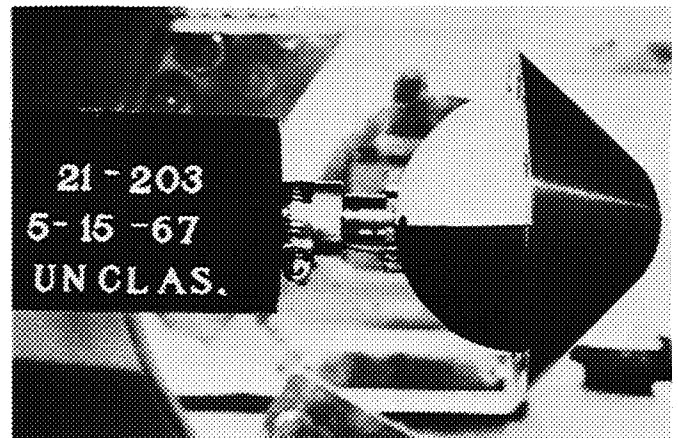
Fig. 26. Typical test setup for dynamic stability test in HWT

frequency of oscillation is inversely proportional to the square root of moment of inertia, considerable care was taken to obtain low moments of inertia so as to have reasonable frequencies.

Table 2. Moments of inertia

Model	I (lbf–in.–s^2)
45-0	0.0085837
45-25	0.0099030
45-50	0.0105410
45-75	0.0099593
45-100	0.0101188

The data were collected through a system that uses an Optron Tracker, a passive electronic device which is designed to follow the motion of an object without physical contact. The tracker requires a target having a sharp delineation in brightness to provide contrast. If the target is not on the model's center of rotation, angular deflection of the model will yield a vertical displacement of the target, and the Optron Tracker output will be a function of the angle of attack of the model. The instrument is calibrated statically by pitching the model to a known angle of attack and recording the output. The relationship between voltage output and model angle of attack is very linear between -30 and $+30$ deg. The data necessary to determine model stability are oscillation amplitude and frequency, both of which are obtained from the output of the Optron Tracker.

Substantial loads on the model lead to sting deflections as the model oscillates. To determine the effects, if any, of this sting motion on the model's oscillatory history, the sting was instrumented with a strain gage bridge which provided a method of determining both loads and deflections. Output from the strain gage bridge was recorded along with data from the Optron Tracker. Sting deflections were insignificant.

Test procedure consisted of checking frictional damping of the gas bearing to ensure that it was negligible. This was done by mounting a low moment of inertia sphere, with an offset mass, on the gas bearing and observing its oscillation in the flow after it had been released from an initial angular deflection. The model was then mounted on the gas bearing and the Optron Tracker calibrated. The test runs were made by releasing the model from an initial angular deflection of 20 deg and allowing the model to oscillate until the motion had damped to approximately 2 or 3 deg. Each model was run four times at the same test conditions to check repeatability.

The test data were reduced on the premise that the pitching moment is linear with angle of attack and the prime contributor to angular velocity. The following equations were used:

$$C_{M_\alpha} = -\frac{4\pi^2 f^2 I}{q_\infty A d} \qquad (2)$$

and

$$C_{M_q} + C_{M_{\dot\alpha}} = \frac{2IV_\infty}{q_\infty A d^2} \frac{1}{t} \ell n \frac{\alpha_t}{\alpha_0} \qquad (3)$$

Pitching moment is not linear with angle of attack over the entire range, but is linear to a good approximation for small angles where the theoretical calculations are expected to apply. The data reduction was performed on a IBM 7090 computer.

A linear curve fit was made to $\log_e \alpha_e$ (envelope angle) as a function of time and this was used in Eq. (3) to calculate $C_{M_q} + C_{M_{\dot\alpha}}$. A typical trace of the run data is shown in Fig. 27. A data-smoothing program was then applied to these data to yield Fig. 28. The data were cut off at 30 s and it can be seen that the curve is quite linear. A third-order polynomial curve fit was made to the data and compared with the linear curve fit. The third-order polynomial fit did not make a significant correction and, therefore, the linear curve fit was used throughout.

Only the amplitude envelope and frequency are necessary for the data reduction. Each test run yields two amplitude envelopes, one for positive alpha peaks and one for negative alpha peaks, which were averaged to eliminate any fictitious alpha reading when the model is trimmed in the flow. Average amplitude envelopes are calculate $C_{M_q} + C_{M_{\dot\alpha}}$.

The dynamic stability coefficient $C_{M_q} + C_{M_{\dot\alpha}}$ versus bluntness ratio is shown in Fig. 29. The open symbols are the linear curve fit of the data and the filled symbols are the averages of these data. The scatter shown is typical of the free oscillation method of testing, since the damping is produced by the unsteady flow field about the vehicle. The apparently greater stability of the 0.50 bluntness ratio over the other blunted cones is as yet unexplained. This phenomenon warrants further study.
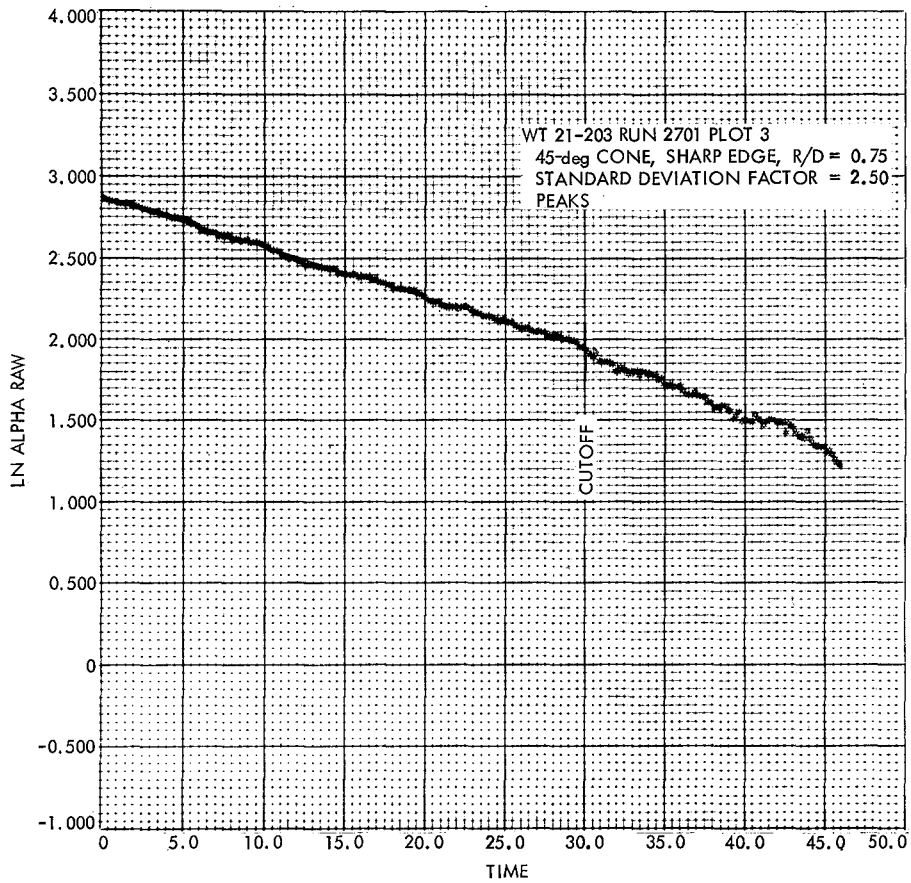
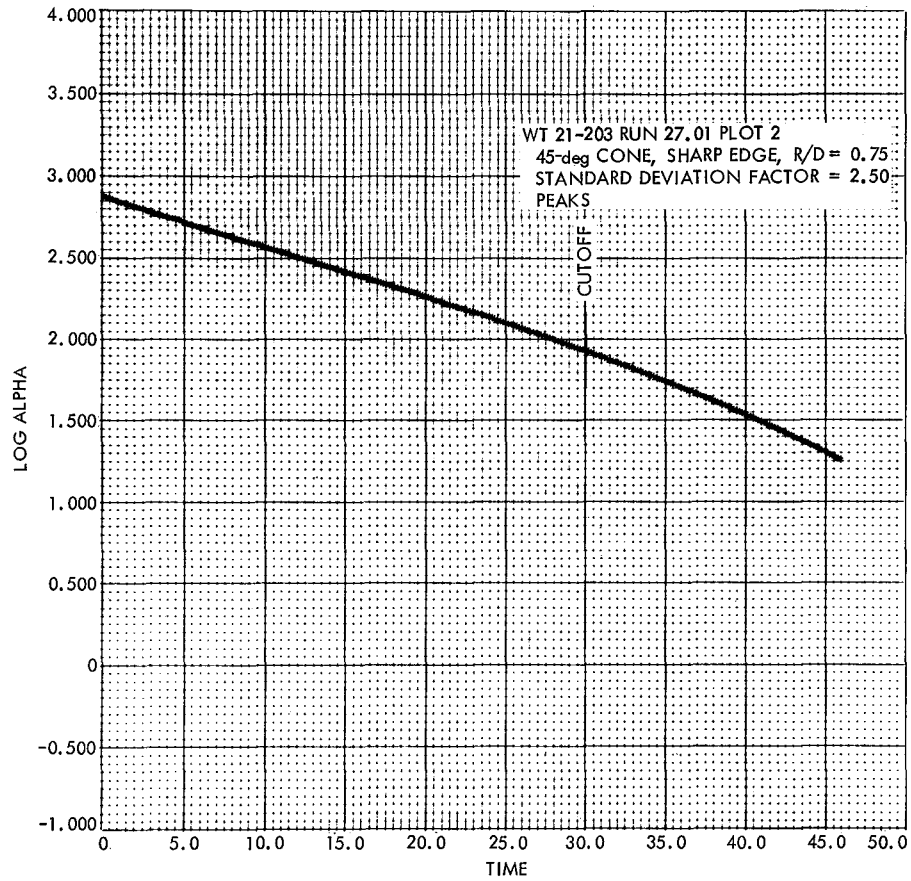Fig. 27. Typical raw data output from Optron Tracker
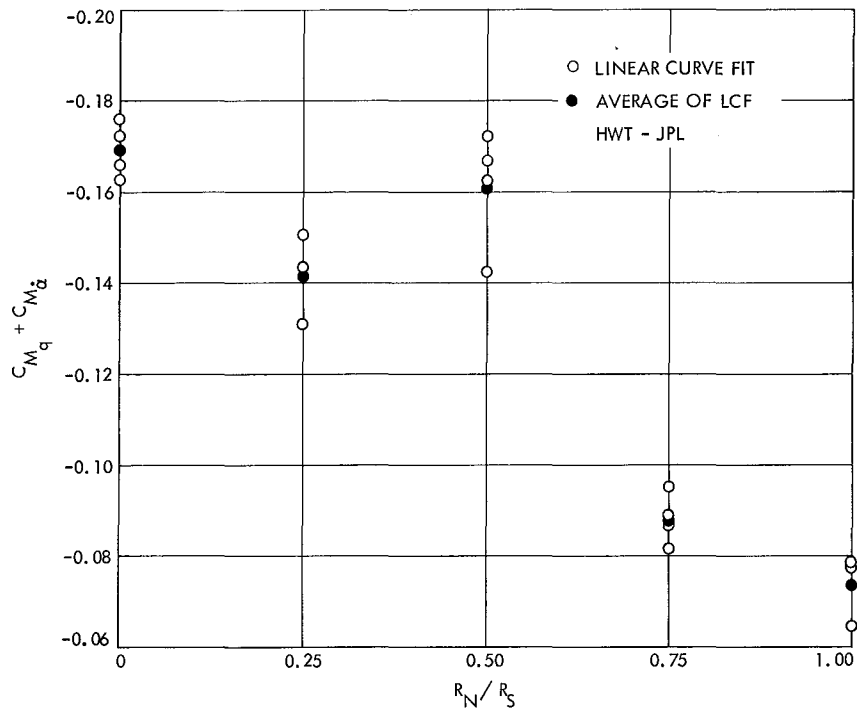
Fig. 28. Typical reduced data from Optron Tracker

Fig. 29. Dynamic stability coefficient, $C_{M_q} + C_{M_{\dot{\alpha}}}$, vs R_N/R_B for an ideal gas
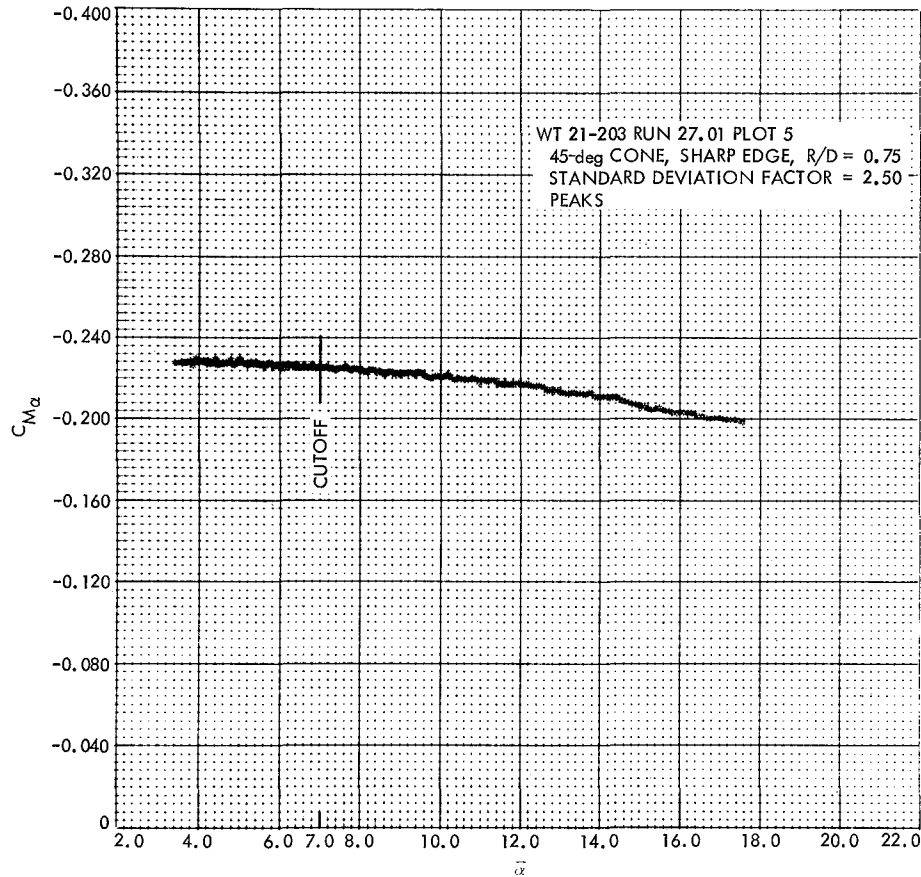
Fig. 30. Typical static stability coefficient, C_{M_α}, vs $\bar{\alpha}$ from dynamic stability test

The mean amplitude of oscillation between α_0 and α_t of Eq. (3), $\bar{\alpha}$, is calculated by

$$\bar{\alpha} = \left(\frac{\alpha_t^2 - \alpha_0^2}{2 \, \ln \frac{\alpha_t}{\alpha_0}} \right)^{1/2}$$

and is approximately equal to

$$\frac{\alpha_0 + \alpha_t}{2}$$

The static stability derivative C_{M_α} varies only slightly over the angle-of-attack range, as can be seen in a typical plot (Fig. 30). The static stability derivative C_{M_α} versus bluntness ratio is plotted in Fig. 31. The $\bar{\alpha}$ used in Fig. 31 is the same as that used in Fig. 29 for $C_{M_q} + C_{M_{\dot{\alpha}}}$, the dynamic stability coefficient.

VI. Comparison of Theory With Experiment

The theoretical pressure distribution for the ideal gas case is compared to the data obtained from pressure measurements of the 45-25 and 45-100 models in the HWT in Fig. 32. The triangles are for the 45-25 model, the circles for the 45-100 model and are generally higher in pressure level. The theoretical curve is slightly low on the spherical segment while it agrees very well on the conical portion. Both the theory and experiment approach the pointed cone value further out on the conical surface, as is to be expected. The theory fails to calculate the pressure on the sphere-cone junction region as well as in the spherical or conical regions. This is the most difficult region for theory to predict because the radius of curvature of the body jumps discontinuously from R_N to infinity.

The theoretical pressure distribution for the real gas case is compared to the data obtained in the EGF for test flows in equilibrium and out of equilibrium in Figs. 33
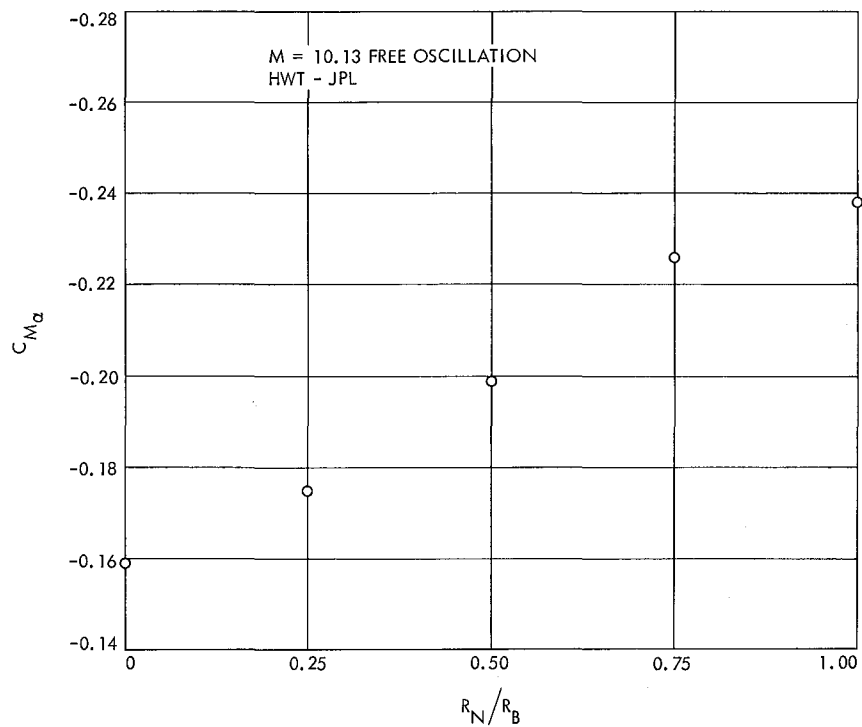
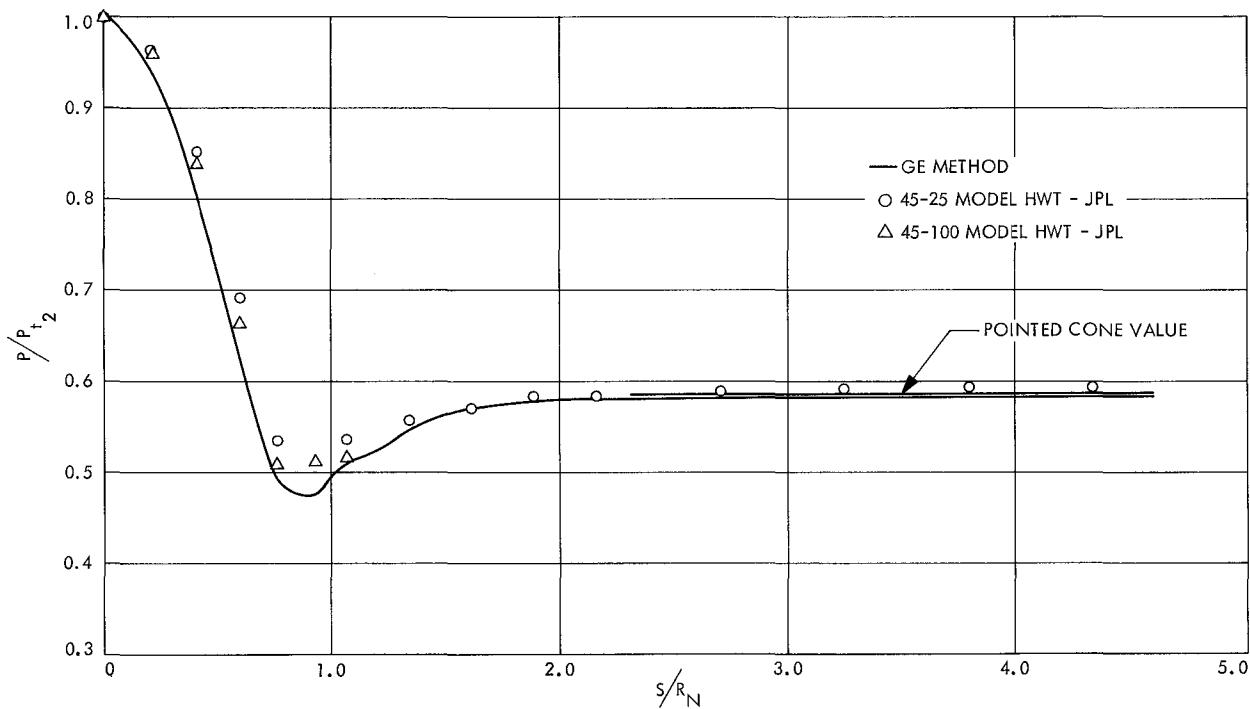Fig. 31. C_{M_α} vs R_N/R_B for an ideal gas

Fig. 32. Comparison of GE theoretical pressure distribution with experiment for an ideal gas
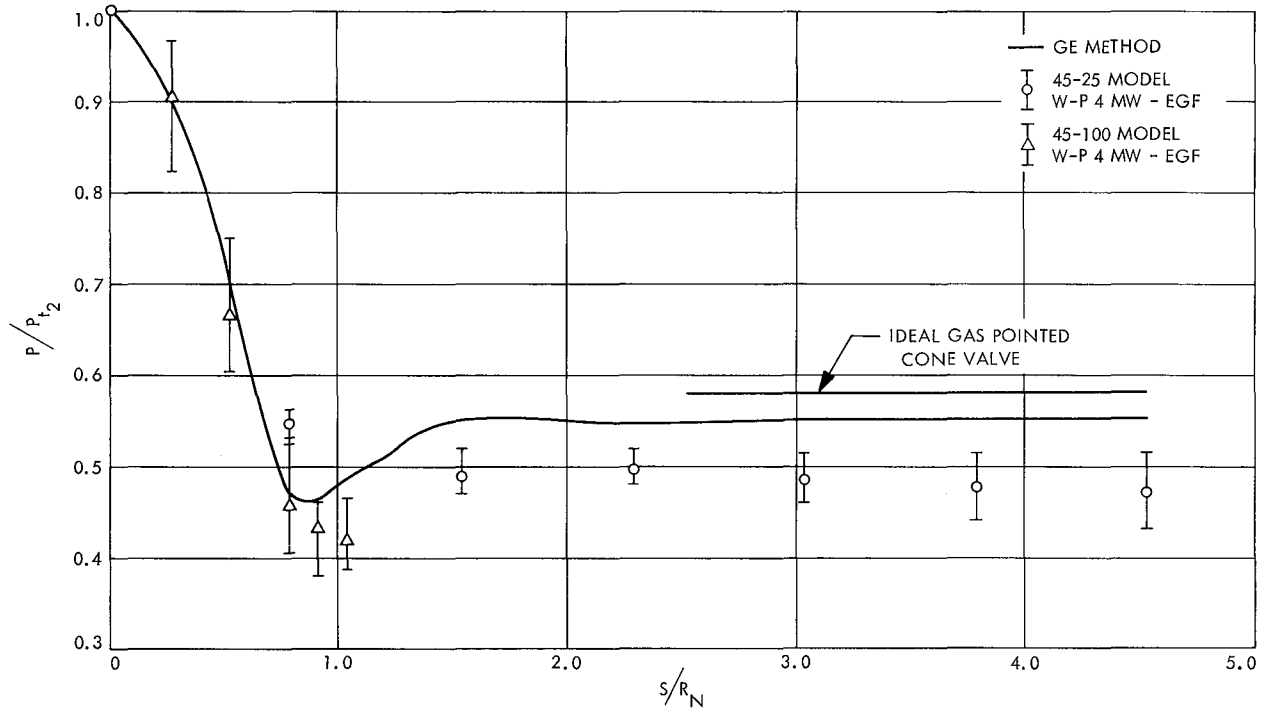
Fig. 33. Comparison of GE theoretical pressure distribution with experiment for a real gas in equilibrium
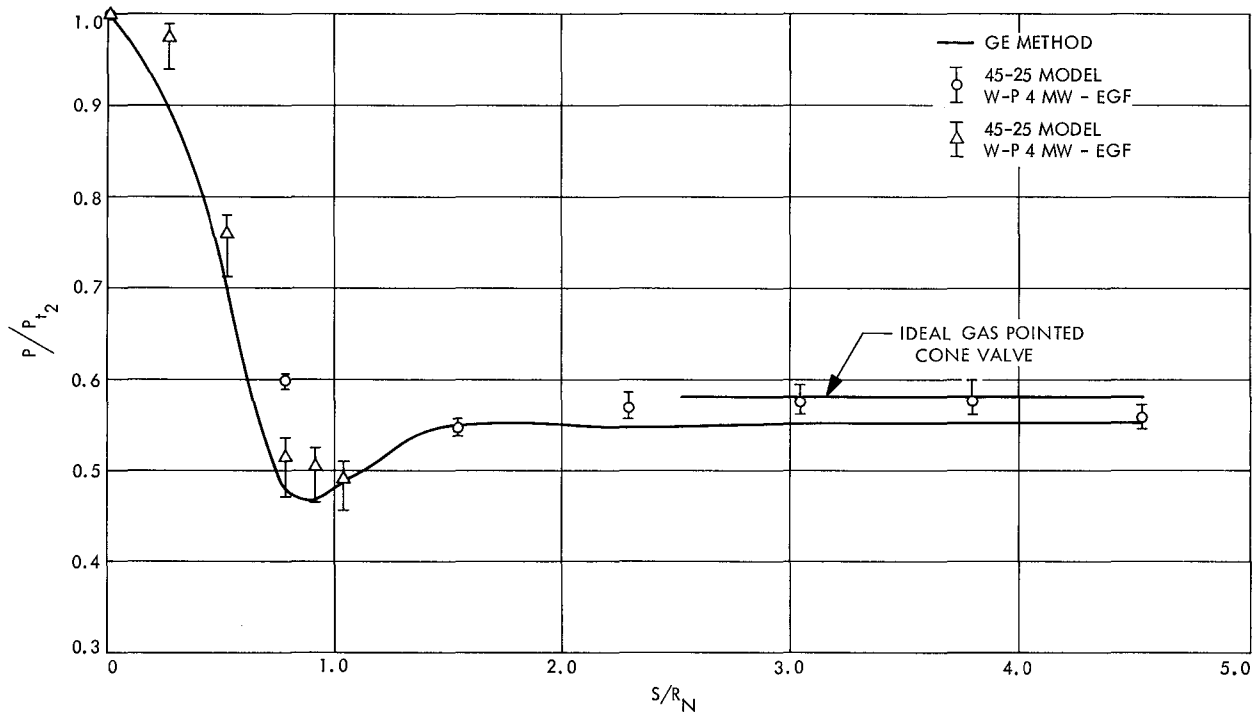

Fig. 34. Comparison of GE theoretical pressure distribution with experiment for a real gas in nonequilibrium

and 34, respectively. Again, the triangles and circles represent the 45-25 and 45-100 models, respectively, whereas the curve is the theoretical calculation. The data scatter shows that the scatter for the equilibrium flow condition is greater than that of the nonequilibrium condition. The testing techniques for both flow conditions were the same and, thereby, no explanation other than general thermochemical effects can be offered as to the reason for the scatter. It should also be noted that the theory compares with the data for the equilibrium flow better than with the data for nonequilibrium flow on the spherical portion of the model, whereas on the conical portion of the model, the opposite is true. In general, the theory compares with the nonequilibrium flow data better than with the equilibrium flow data. A possible explanation is that the gas in the shock layer may not be in equilibrium for the near-equilibrium test flow. Also, for the nonequilibrium test flow condition, the gas in the shock layer could have been shocked to a near-equilibrium condition. Therefore, it is possible that the nonequilibrium flow could yield better flight simulation than the equilibrium flow.

The normalized rate of change of pressure with respect to alpha at zero angle of attack, $1/P_{t_2} \partial P/\partial \alpha \mid_{\alpha=0}$, is shown in Figs. 35, 36, and 37 for the ideal gas case, real gas case in equilibrium, and real gas case in nonequilibrium, respectively. The theoretical and experimental data are shown for roll angles of 0, 30, 60, and 90 deg. The theoretical calculation for the ideal gas case compares very well with the experimental data obtained from the HWT. A comparison between Figs. 35 and 9 shows that the theory represents an improvement over the Newtonian value. The data in Figs. 36 and 37 are too uncertain to make any judgment of the theory's capability of predicting a real gas pressure derivative. The uncertainty is indicated in the pressure derivative at $\phi = 90$ deg. The derivative should be zero at this roll angle as in Fig. 35 for the ideal gas case.

The axial force coefficient for an ideal gas is shown in Fig. 38. The data are those of Ref. 5. Because of lack of data, it is difficult to draw a definite conclusion as to the validity of the theory; however, for the two data points given the theory seems to be in fairly good agreement.
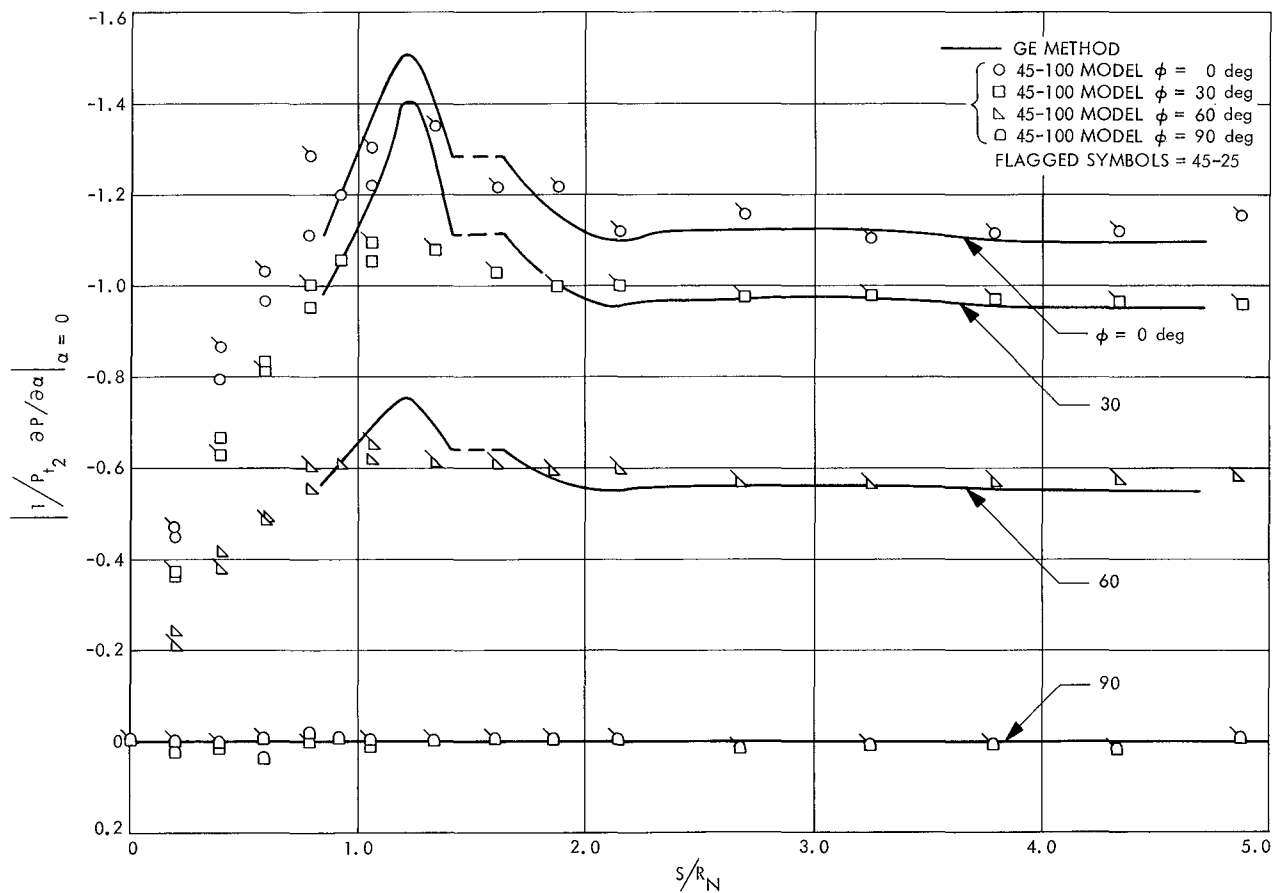

Fig. 35. Comparison of GE theory for $1/P_{t_2} \partial P/\partial \alpha \mid_{\alpha=0}$ vs S/R_N with experiment for an ideal gas

Fig. 36. Comparison of GE theory for $1/P_{t_2} \partial P/\partial\alpha \big|_{\alpha=0}$ **vs** S/R_N **with experiment for a real gas in equilibrium**
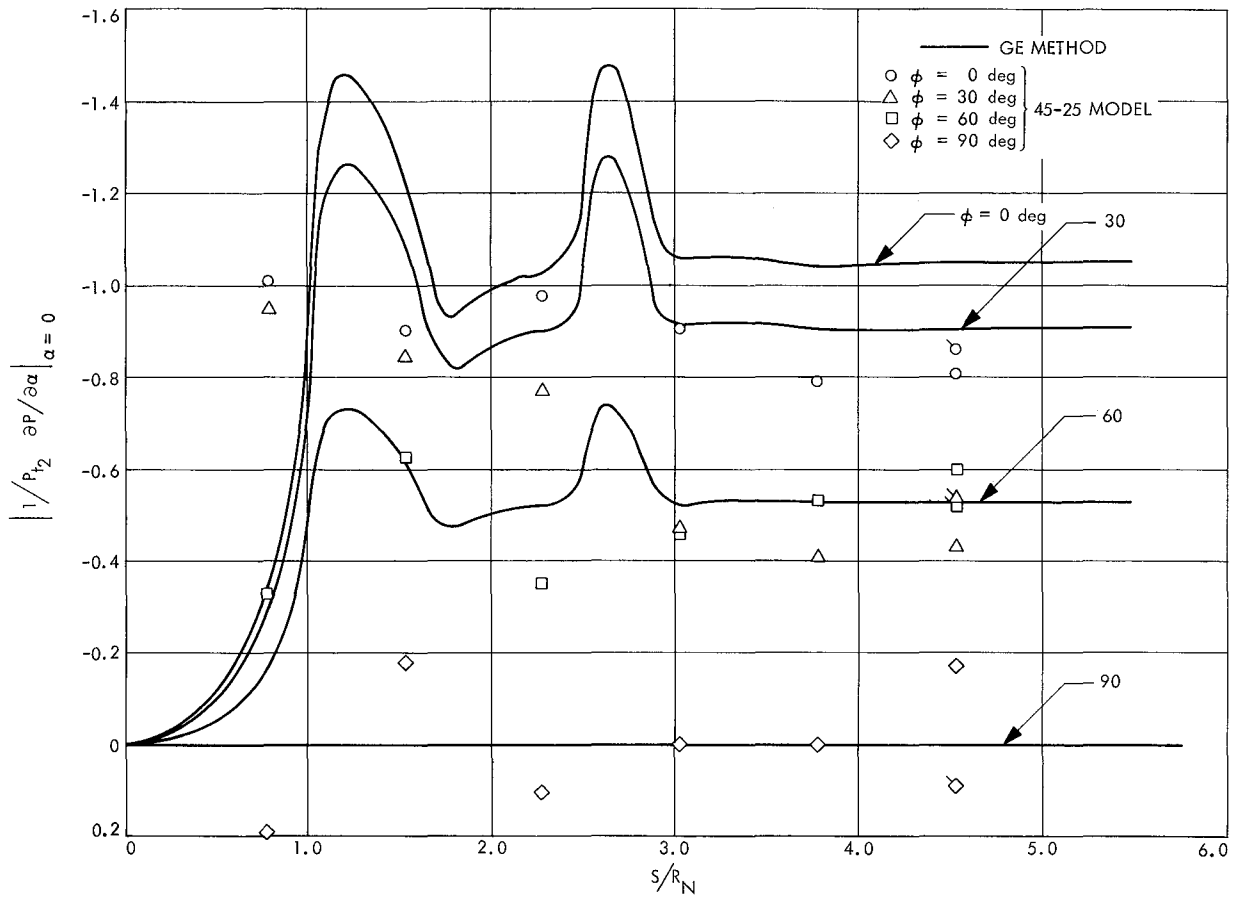
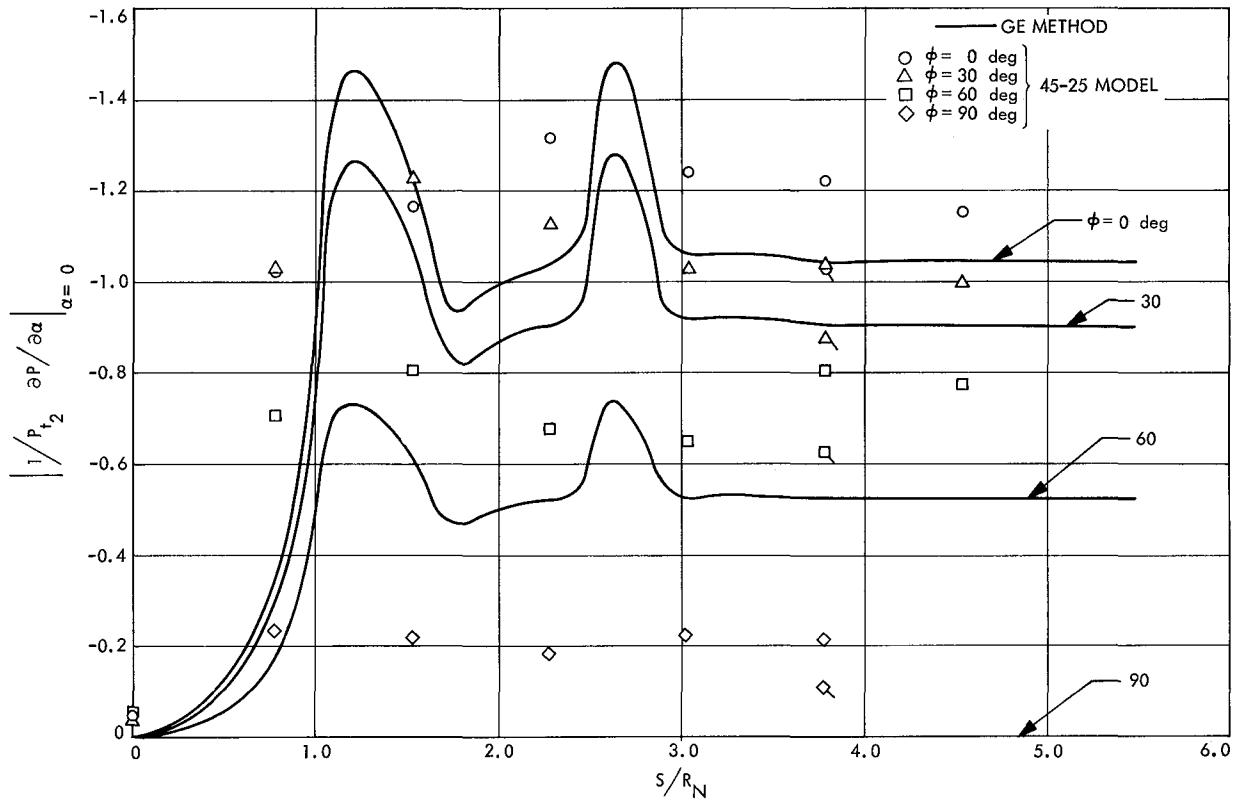Fig. 37. Comparison of GE theory for $1/P_{t_2} \partial P/\partial \alpha \big|_{\alpha=0}$ vs S/R_N with experiment for a real gas in nonequilibrium
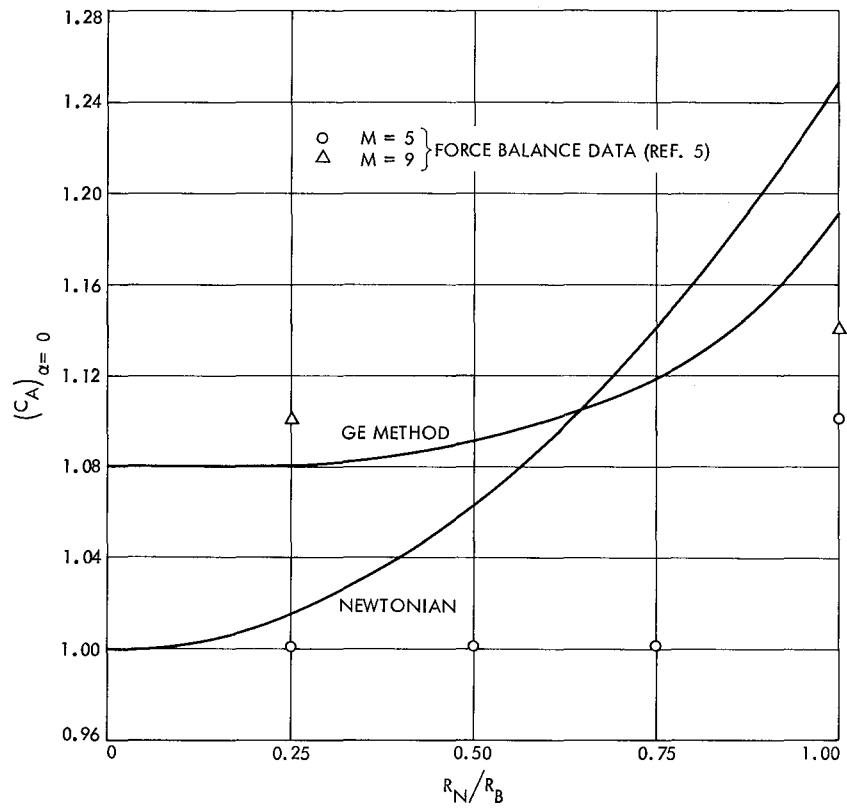
Fig. 38. Comparison of GE theory for $C_A \big|_{\alpha=0}$ vs R_N/R_B with experiment and Newtonian theory for an ideal gas
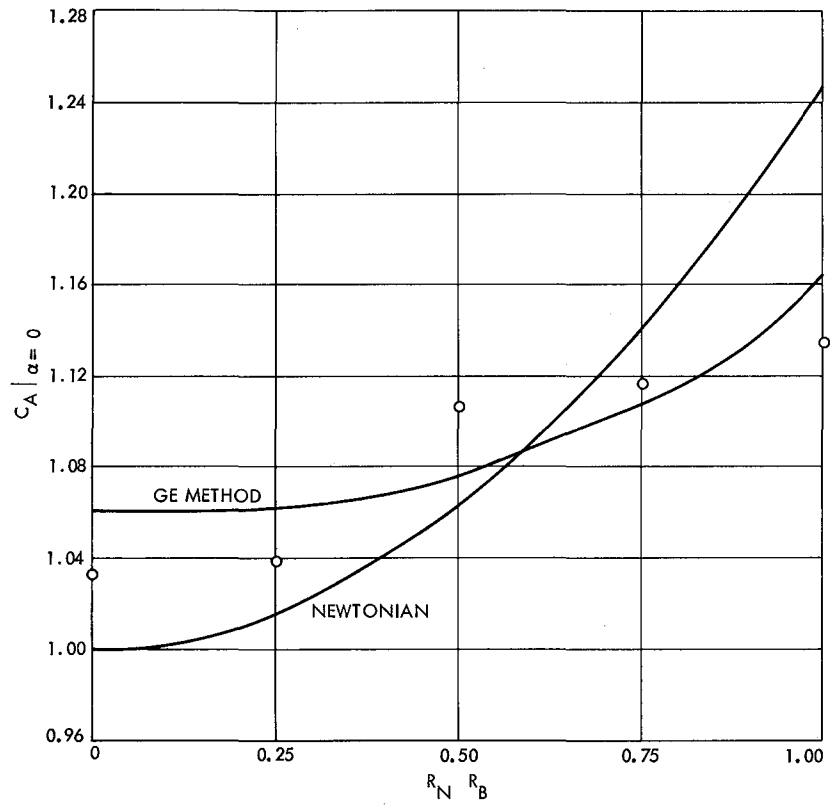
**Fig. 39. Comparison of GE theory for $C_A \mid_{\alpha=0}$ vs R_N/R_B
with experiment and Newtonian theory for
a real gas in equilibrium**

The theory also represents an improvement over the Newtonian theory if one is willing to put that much weight on this limited data. The axial force coefficient for the real gas case in equilibrium is given in Fig. 39. The data are given in Fig. 23 with the appropriate scatter bars. The theory agrees fairly well with the data and predicts the data better than the Newtonian theory. This result also gives support to the theory for the ideal gas.

The normal force coefficient slope for an ideal and real gas in equilibrium is shown in Figs. 40 and 41, respectively. These curves were obtained from figures such as Fig. 24. Again, data from Ref. 5 are used for the comparison of the theory for the ideal gas case. Although the data are not complete enough to draw conclusions for the theory in the ideal gas case, the conclusions for the real gas case are obvious: the theoretical calculation is a significant improvement over that of the Newtonian theory. Similar conclusions would have been drawn for the ideal gas case had the data been more complete.

Figures 42 and 43 show the static stability coefficients that were obtained from figures such as Fig. 25. Data for the ideal gas case is from the dynamic stability test as well as Ref. 5. Unlike the previous results, the Newtonian theory predicts the data better than the theoretical calculation. This also seems to be the case for the real gas case (Fig. 43); however, the data have some scatter which makes any observation difficult.

The dynamic stability coefficient, $C_{M_q} + C_{M_{\dot{\alpha}}}$, is shown in Fig. 44. The Newtonian values shown are for C_{M_q} only. Since $C_{M_{\dot{\alpha}}}$ is generally much smaller than C_{M_q}, the use of C_{M_q} for the dynamic stability coefficient is slightly conservative. The GE theory is an improvement over the Newtonian theory although it seems to be overlooking some important contribution to the coefficient; i.e., the theory falls down for the sharp cone and cone of 0.50 bluntness ratio. As previously stated, no dynamic stability data were obtained for the real gas case because of tunnel limitations in the EGF.

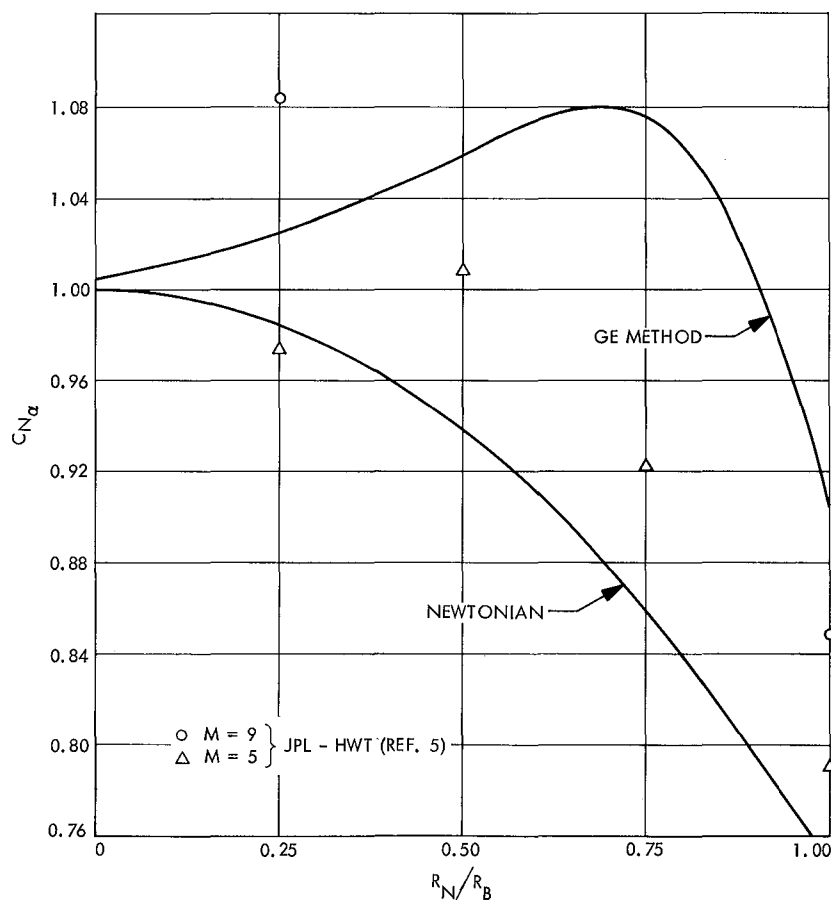Fig. 40. Comparison of GE theory for C_{N_α} vs R_N/R_B with experiment and Newtonian theory for an ideal gas
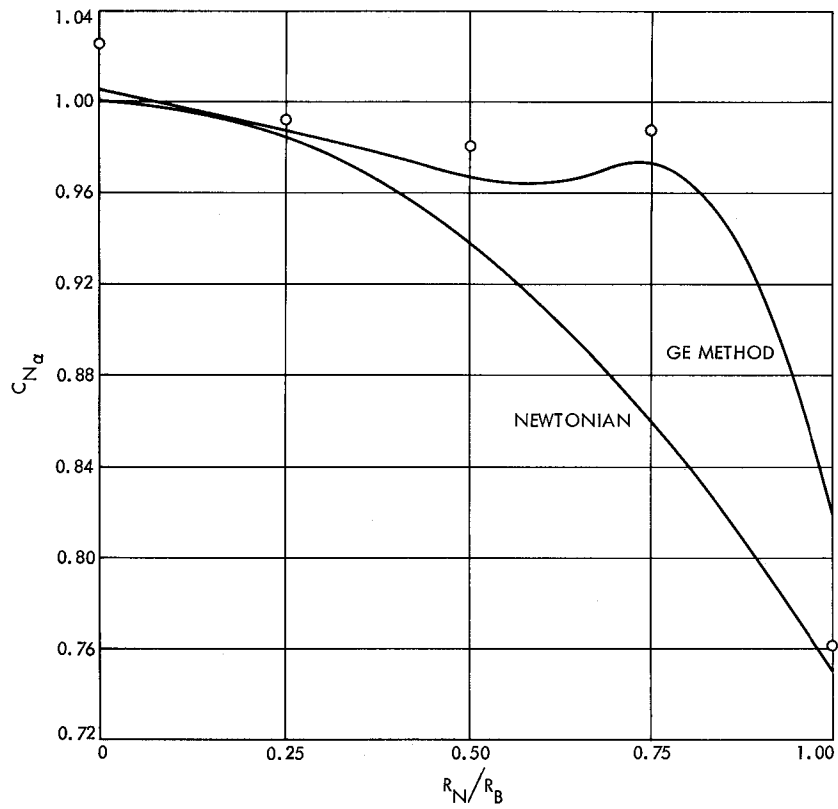
Fig. 41. Comparison of GE theory for C_{N_α} vs R_N/R_B
with experiment and Newtonian theory
for a real gas in equilibrium
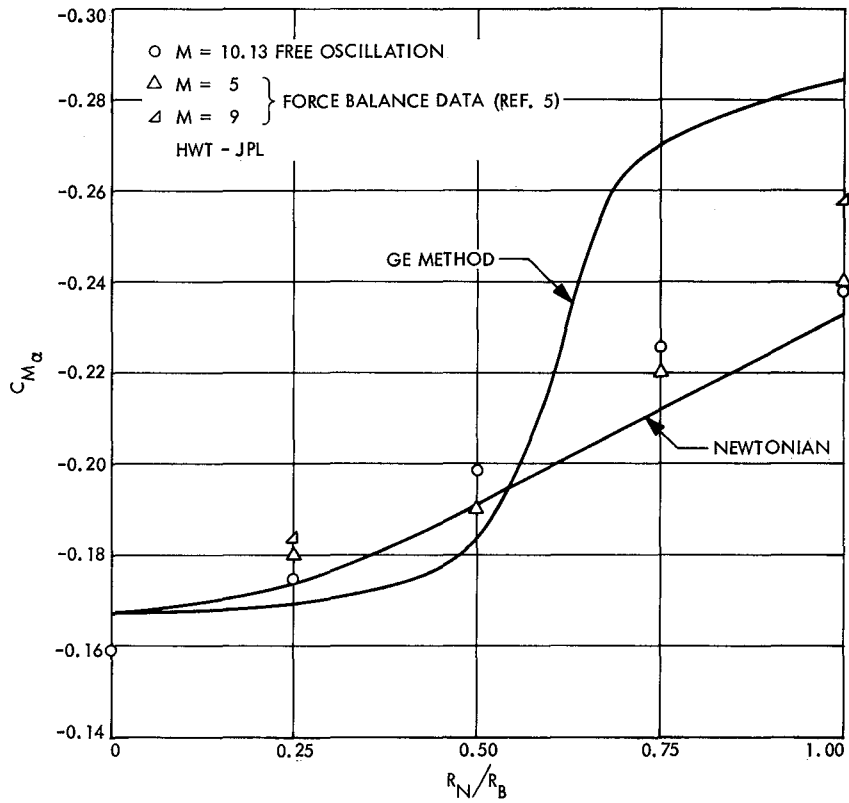
Fig. 42. Comparison of GE theory for C_{M_α} vs R_N/R_B with experiment and Newtonian theory for an ideal gas
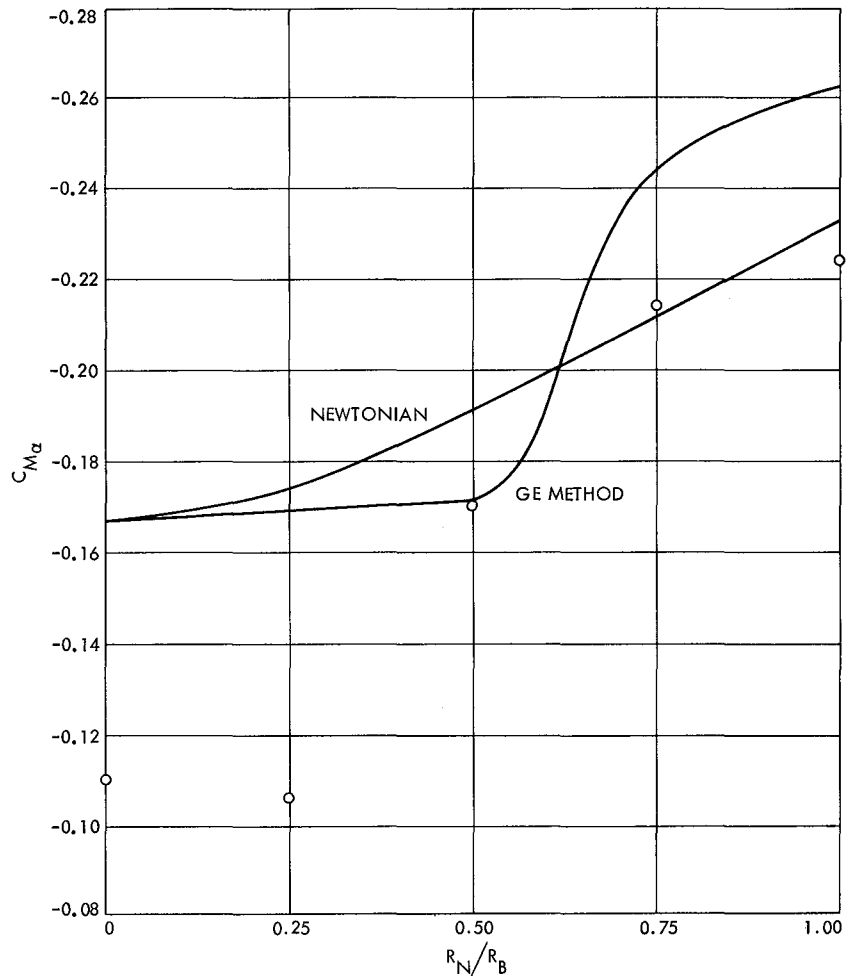
Fig. 43. Comparison of GE theory for C_{M_α} vs R_N/R_B
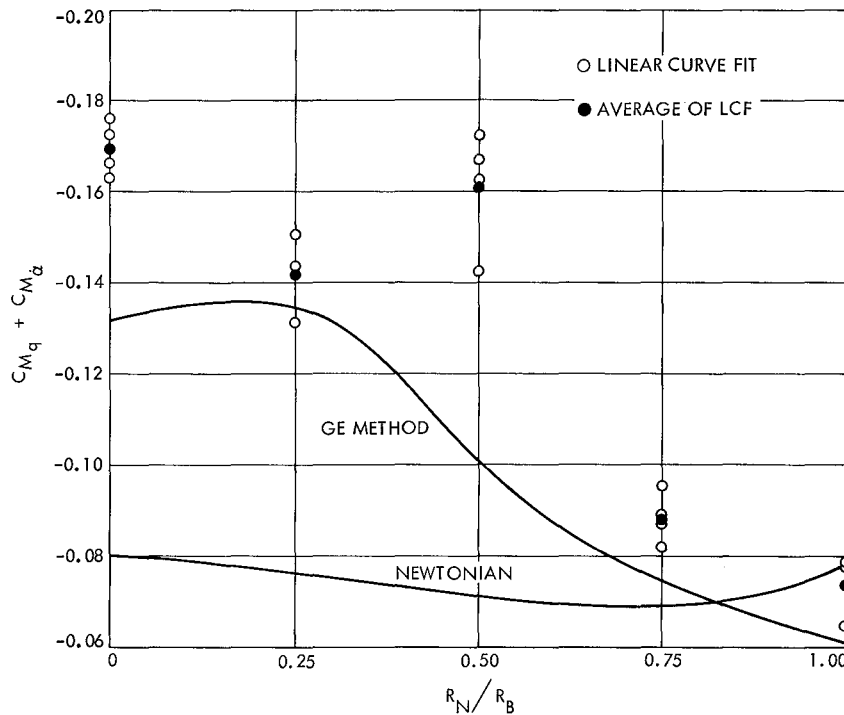with experiment and Newtonian theory
for real gas

**Fig. 44. Comparison of GE theory for dynamic stability
vs R_N/R_B with experiment and Newtonian
theory for an ideal gas**

The GE theory generally does predict coefficients better than the Newtonian theory with the exceptions previously pointed out.

VII. Summary

The GE theory represents a significant improvement in the prediction of pressure distribution and stability coefficients over that predicted by Newtonian theory, with the exception of the static stability coefficient, $C_{M_{\dot\alpha}}$. Although the dynamic stability coefficient, $C_{M_q} + C_{M_{\dot\alpha}}$, is predicted much better for an ideal gas than the Newtonian theory, there is still need for improvement. It is for this reason that the theoretical calculation of the dynamic stability coefficient for the real gas in equilibrium would have an uncertainty associated with it. This comparison of the GE theory with experimental data has given some guidelines of applicability and, it is hoped, will stimulate further investigations along these lines.

References

1. Brong, E. A., "The Flow Field About a Right Circular Cone in Unsteady Flight," Paper No. 65-398, presented at the AIAA Second Annual Meeting, San Francisco, Calif. July 26–29, 1965.

2. Brong, E. A. and Rie, H., "The Flow Field About Pointed and Blunt Bodies of Revolution in Unsteady Supersonic Flight," *Trans. of the Second Technical Workshop on Dynamic Stability Testing* held at the Arnold Engineering Development Center, Arnold Air Force Station, Tenn., April 20–22, 1965.

3. Kyriss, C. L. and Rie, H., "Theoretical Investigation of Entry Vehicle Stability in the Mars Atmosphere," *J. Spacecraft Rockets,* Vol. 4, No. 2, pp. 272–275, Feb. 1967.

4. *"Flow Field Computations for Blunt Bodies in Planetary Environments (Equilibrium),"* Modification No. 1, Final Report, JPL Contract No. 951647–Supplement, General Electric Company, Jan. 5, 1968.

5. Nichols, J. and Nierengarten, E., *"Static Aerodynamic Characteristics of Blunted Cones and Round-Shouldered Cylinders Suitable for Planetary Entry Vehicles at a Mach Number Range 1.65 to 9.00,"* Wind Tunnel Report 20-558, Jet Propulsion Laboratory, Pasadena, Calif., Feb. 15, 1964.

6. Zonars, D., "Theoretical and Experimental Study of Equilibrium and Non-Equilibrium Air Flow Through a Mach Number 10 Contoured Nozzle," Paper No. 66-2, presented at the AIAA Third Aerospace Sciences Meeting, New York, Jan. 24–26, 1966.

7. Parobek, D. M., *"Performance of Free Stream Flow Instrumentation for 9-Inch Contoured Nozzle Test in the RTD 4-Megawatt Electro-Gasdynamic Facility,"* Report AFFDL-TR-65-179, Air Force Flight Dynamics Laboratory, Dec., 1965.

8. Petrie, S. L. and Gregorek, G. M., *"A Summary of Similitude Studies for High Enthalpy Hypersonic Test Facilities,"* Report AFFDL-TR-66-74. The Ohio State University Research Foundation, Air Force Flight Dynamics Laboratory, Sept., 1966.

9. Jorgensen, L. H. and Gayle, B. M., *"Charts for Equilibrium Flow Properties of Air in Hypervelocity No. 22LES,"* Report TN D-1333, Ames Research Center, National Aeronautics and Space Administration, Sept., 1962.

10. Prislin, R. H., *"Free-Flight and Free-Oscillation Techniques for Wind Tunnel Dynamic-Stability Testing,"* Technical Report 32-878, Jet Propulsion Laboratory, Pasadena, Calif., March 1, 1966.